



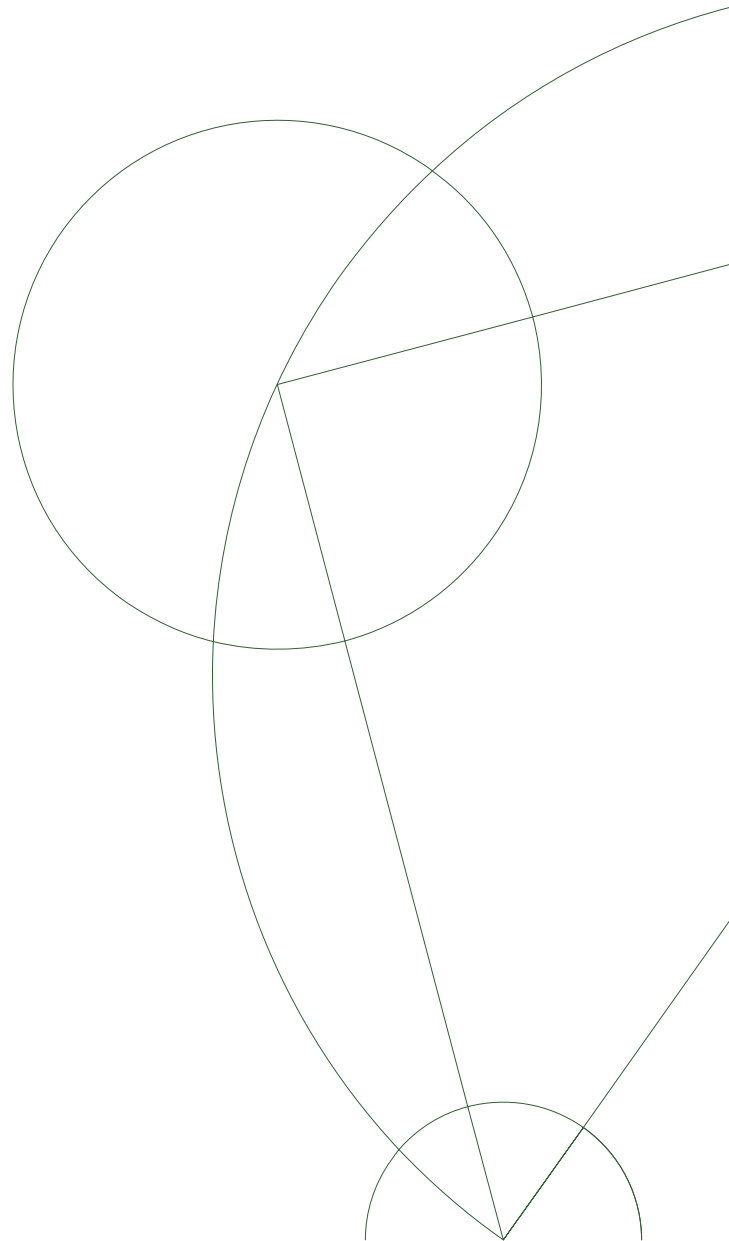
Master's Thesis

Jacob Svensmark

Effect of asphericity in caustic mass estimates of galaxy clusters

Academic advisor: Assoc Prof Steen H. Hansen

Submitted: June 3, 2014



Contents

1	Introduction	3
1.1	The nature of galaxy clusters	3
1.2	Methods of mass estimation	4
1.2.1	Dynamical mass through the virial theorem	5
1.2.2	Dynamical mass through the Jeans equation	5
1.2.3	Non-dynamical masses	6
1.3	Aspherical clusters and thesis objectives	7
2	Asphericity and the caustic technique	9
2.1	Simulations and mock catalogues	9
2.2	Stacking the data	10
2.2.1	Ellipsoidal geometry and alignment	10
2.2.2	Filament geometry and alignment	10
2.2.3	Spherical reference geometry	11
2.3	The caustic technique	12
2.3.1	Phase space density distribution	12
2.3.2	Caustic amplitude and gravitational potential	13
2.4	Results	13
2.5	Discussion	17
2.5.1	Low mass bin	20
2.5.2	High mass bin	22
2.5.3	Triaxiality	22
2.6	Conclusion	23
2.7	Outlook	24
3	Appendix	27

Abstract

The caustic technique of mass estimation of galaxy clusters relies on the assumption of spherical symmetry, which is not always a valid assumption. Here we demonstrate the effect of spatial anisotropy of galaxy clusters on the inferred caustic mass profiles by studying mock observational data generated from dark matter N -body simulations. We find a factor of ~ 2 discrepancy between major and minor axis mass estimates in ellipsoidal clusters within the virial radius R_v , and up to ~ 3 within $3 R_v$. We also find filaments to influence caustic mass estimates at a significant magnitude.

By stacking halos to align their principal axes we find that a line of sight along the major axis overestimates the caustic mass of galaxy clusters, as well as a line of sight along the minor axis underestimates it. The mass discrepancy between the major and minor axis is a factor of 1.72, 1.95 and 2.44 at 1, 2 and $3 R_v$ for virial masses within $(1 - 2) \times 10^{14} h^{-1} M_\odot$, and (14 – 20)% larger for $\geq 2 \times 10^{14} h^{-1} M_\odot$. By stacking halos to instead align their largest associated filament we find a mass overestimation with line of sight nearly along the filament, and an underestimation with line of sight orthogonal to the filament. For the low mass bin we find a factor of 1.22, 1.49 and 1.71 discrepancy within 1, 2 and $3 R_v$ between line of sight along and across the filament, and a (1 – 19)% smaller discrepancy for the high mass bin. Furthermore, we find no significant bias due to ellipsoidal structure ($< 8\%$). We provide useful tables which can be used to estimate mass discrepancy when cluster orientation is known.

Chapter 1

Introduction

1.1 The nature of galaxy clusters

On the very largest of scales to a good approximation the universe can be considered a homogeneous and isotropic medium of mainly dark matter and energy, with a small trace of baryonic matter added into the mixture. Homogeneity and isotropy constitute the two fundamental and observationally well founded assumptions of cosmology. The current distribution of matter and energy is a descendant of a pre-historical energetically dense medium which through a brief period of rapid and violent inflation and through subsequent expansion has evolved into the current state that is our universe. On slightly smaller scales, at ~ 100 Mpc, elaborate and localized structure emerges, and the fundamental cosmological assumptions start to break down. The matter component is distributed through a delicate network of over- and underdense regions, progeny to a weak quantum noise in the pre-historical state frozen in by inflation, and enhanced by gravity and time. Along these overdense regions is where galaxies have formed. Often galaxies form in regions of the highest concentrations, and thus tend to cluster together in groups. Clusters of galaxies place themselves as structural 'knots' in the context of this network of overdensity commonly referred to as 'the cosmic web' or 'the large scale structure' (see Fig. 1.1). Clusters are interconnected by the less dense string-like 'filaments' and plane-like 'sheets' of matter and together they encapsulate the under dense cosmic voids which in terms of volume take up most of the universe.

As manifestations of the most massive gravitationally bound objects of our universe clusters of galaxies yield fascinating properties. They are multi-component systems with masses measured between $\sim 10^{14} M_{\odot}$ and up to $\sim 10^{15} M_{\odot}$. Of this mass, the majority ($\sim 90\%$) is in the form of dark matter, and of the remaining baryonic component $\sim 90\%$ takes the form of hot ionized gas. Only a few % of the total mass is in the form of stellar matter found in the collection of 50 – 1000 member galaxies that historically have given name to the objects. Observationally clusters are visible through a broad range of channels. Their resident galaxies contribute much at optical and near infra-red wavelengths as exemplified in the left side of Fig. 1.2 for the Abell 1689 cluster. The image is observed by the Hubble telescope, and shows a large number of clustered yellow galaxies, as well as blue and red background galaxies. Additionally at these wavelengths clusters may act as gravitational lenses for light emitted by background sources, visible observationally as round light arcs and background image distortion. The Abell 1689 cluster of Fig. 1.2 shows clear both lensing arcs and background distortion, bearing witness to its large mass. The hot gas of the intra cluster medium emits thermal bremsstrahlung in X-ray regime. An example of this can be seen in the X-ray image on the right side of Fig. 1.2 for the Abell 2597 cluster. Finally at millimetre wavelengths inverse Compton scattering on high energy electrons from the hot gas component distorts the cosmic microwave background to produce an observable signature. All of this spectral information allows for detailed analysis of the nature of galaxy clusters, and thus has given rise to a large field of study within astrophysics and cosmology.

Though interesting on their own, one of the main motivations of studying the properties of galaxy clusters comes from their ability to constrain a number of cosmological parameters and test cosmological models and models of general relativity. A main factor in this ability comes via the cluster mass. Within a bin in redshift z and mass M different cosmological models predict a number $N(z, M)$ of clusters within some

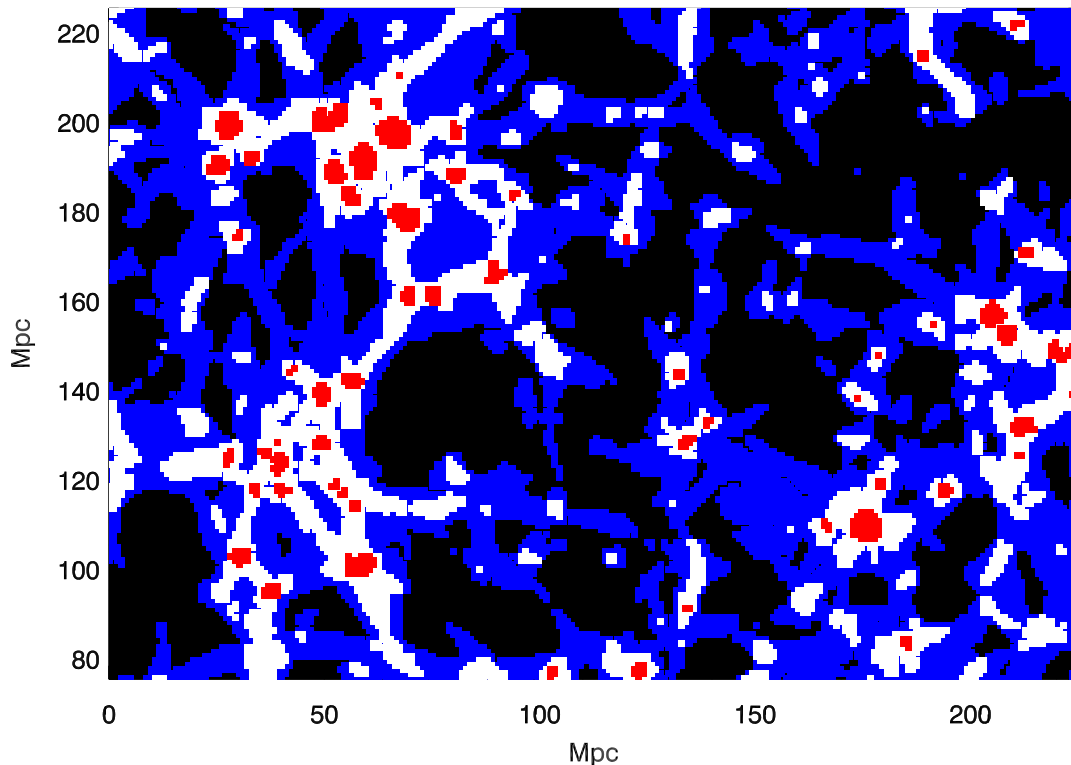


Figure 1.1: The cosmic web as obtained from the Bolshoi N -body simulation described in later sections of this thesis. The figure shows a $225 \times 150 \times 3$ Mpc slice through the simulation at redshift $z = 0$. The black color indicates volume categorized as 'void', the blue color indicates places of 'sheet', the white color indicates 'filaments' and the red color indicates clusters or 'knots'. Classifications are based on a velocity shear tensor map obtained from the Multidark Database, also described in later sections of this thesis.

volume, and knowing the true cluster distribution through observational counts thus allows for testing of these models (Vikhlinin et al., 2009). Other techniques constraining cosmological parameters are the growth rate of clusters (Mantz et al., 2010; Rapetti et al., 2010; Mantz et al., 2014) and the gas mass fraction (Allen et al., 2002). Naturally this calls for methods of estimating the mass of clusters to a reasonable precision. Whilst much of the pioneering work has been done to develop methods capable of obtaining good mass estimates of the objects, our era of precision cosmology calls for constraints on cosmological parameters tighter than what is currently possible. Large amounts of data becoming available both from observations (see the e.g. Sloan Digital Sky Survey (Ahn et al., 2014)) and simulations (e.g. the Millennium Simulation (Springel et al., 2005), Bolshoi simulation (Klypin et al., 2011) and Illustris simulation (Vogelsberger et al., 2014)) also permits the extension of previous efforts. Therefore it is of critical importance to further develop mass estimation techniques to take into account what little uncertainty, scatter and bias that still affects current observations. For more information on galaxy clusters as cosmological probes see review by (Allen et al., 2011).

1.2 Methods of mass estimation

Much of the current methodology is formulated within a spherical framework. The very definition of cluster mass is usually formulated in terms of spherical overdensity, which locates centres of highest concentration

and evaluates the density within spheres of increasing size against a background density. Choosing a typical $\Delta = 100$ and the background density to be the critical density ρ_{crit} , the cluster mass M_Δ is that contained within a sphere of radius R_Δ such that $3(M_\Delta)/(4\pi R_\Delta^3) = \Delta \rho_{crit}$. As such the mass definition is spherical by construction. This naturally fits well with the employment of spherical assumptions in many of the available mass estimators, however as shall later be discussed it fits poorly with the actual matter distribution of galaxy clusters, and as such gives rise to systematic uncertainty in any mass estimates currently available.

For the category of mass estimation methods often labeled as 'dynamical' the input observables are usually limited to the two angular positional coordinates on the sky, and the redshift of each of the member galaxies. This of course amounts to only half the components of the full 6-dimensional phase-space of position \mathbf{x} and velocity \mathbf{v} , and as such, any dynamical method relies at least on some assumptions of cluster geometry. To illustrate how this works, two simple dynamical mass estimators are discussed below.

1.2.1 Dynamical mass through the virial theorem

One of the simplest dynamical mass estimators is obtained by invoking the virial theorem. Assume that an equilibrated system of N galaxies with total mass $M_{tot} = \sum m_i$ is bound with some average velocity $\langle v^2 \rangle = \sum m_i v_i^2 / M_{tot}$, where $v_i^2 = |\mathbf{v}_i|^2$ is the velocity of the i 'th galaxy, and m_i is its mass. The virial theorem states that the total kinetic energy of the system is related to the total potential energy through $K.E. = -\frac{1}{2}P.E.$. In our system we have

$$K.E. = \frac{1}{2} \sum_i m_i v_i^2, \quad P.E. = -\frac{1}{2} \sum_{i \neq j} \frac{G m_i m_j}{r_{ij}}, \quad (1.1)$$

where r_{ij} is the 3D separation between the i 'th and j 'th particle. If then one defines the size of the system as

$$R_G = 2M_{tot}^2 \left(\sum_{i \neq j} \frac{m_i m_j}{r_{ij}} \right)^{-1} \quad (1.2)$$

then the virial theorem states using the above that

$$M_{tot} = \frac{R_G \langle v^2 \rangle}{G}. \quad (1.3)$$

The velocity dispersion along the line of sight is a measurable quantity, as well as some effective radius of the system. By taking into account the projection effects by assuming a spherical distribution of the system observed, equation (1.3) can be used to estimate the mass of a cluster of galaxies. This however requires assumptions about the distribution of matter both in space and velocity. Furthermore, the quantity R_G is no easily observed parameter, and thus this method may easily be subject to systematic uncertainty. Finally the above contains only masses of the particles of the dynamical system i.e. the galaxies, which as mentioned earlier amount to only a few % of the full cluster mass.

1.2.2 Dynamical mass through the Jeans equation

Another simple strategy which does yield a total mass measure of a gravitating system comes through the spherical Jeans equation for non-rotational equilibrated systems. Through a relatively straightforward derivation one can show that

$$M_{tot}(r) = -\frac{r\sigma_r(r)}{G} \left[\frac{d \ln \sigma_r^2}{d \ln r} + \frac{d \ln \nu}{d \ln r} + 2\beta \right], \quad (1.4)$$

where $\nu(r)$ is the galaxy number density, $\sigma_r(r)$ is the radial velocity dispersion in 3D and β is the velocity anisotropy parameter (Binney & Tremaine, 2008). This equation is useful because one can measure the RHS quantities (except β) through assumptions of the three dimensional structure of a galaxy cluster for only its galaxy component, and obtain the total mass (i.e. including dark matter and gas) on the LHS. It is important to point out that this expression assumes multiple properties of the system, with the most important ones

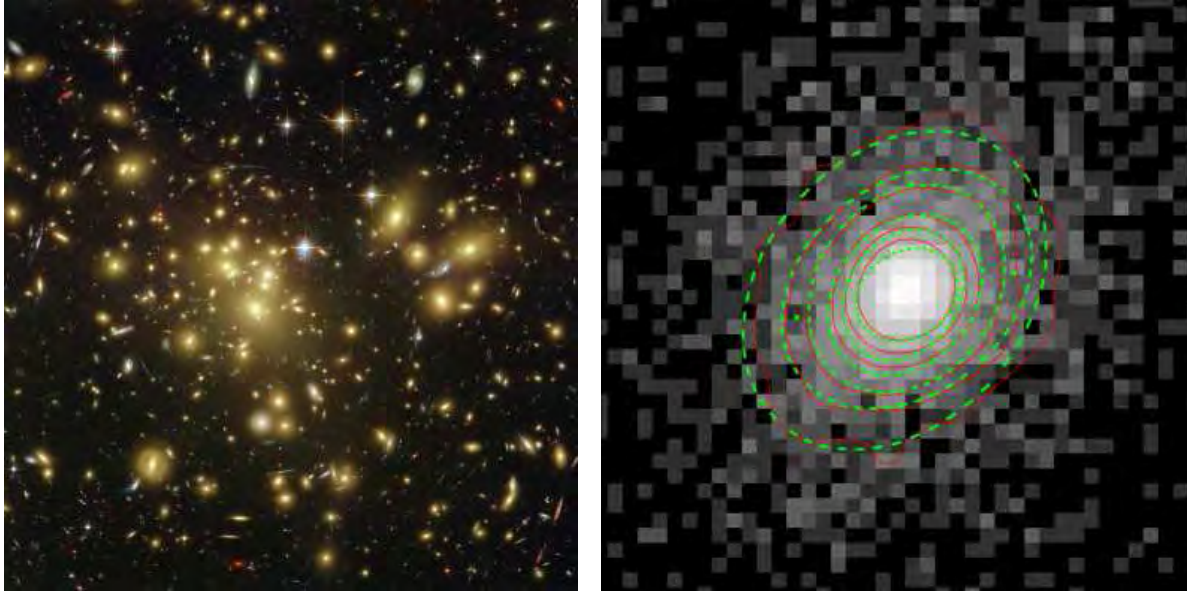


Figure 1.2: *Left:* Optical image of the A1689 galaxy cluster as measured by the Hubble telescope. Both a large number of member galaxies as well as clear lensing arcs are visible. The image was obtained from <http://hubblesite.org/>. *Right:* X-ray image of galaxy cluster A2597 as measured by ROSAT. The isophotal contours are shown in red, and fitted ellipsoids are shown in green. The pixel size is 22.7 kpc. Clear asphericity is visible. The image is obtained from Fig. 2 of Lau et al. (2012).

for this study being the spherical and equilibrated conditions. These assumptions are necessary as it allows for the removal of several terms of the collisionless Boltzmann equation to arrive at the simple form that is equation (1.4).

1.2.3 Non-dynamical masses

Many mass estimators outside of the dynamical regime are also forced to employ assumptions about the state and 3-dimensional distribution of cluster matter due to the limited information available. This despite the fact that clusters are widely represented in the electromagnetic spectrum. Below, we briefly consider some of the most competitive mass estimation methods available, along with their assumptions and potential drawbacks.

X-ray The hot ionized gas that resides inside clusters emits bremsstrahlung in the X-ray regime which yields a radial temperature profile. By assuming the hot gas to be in hydrodynamical equilibrium with the rest of the cluster components, and by assuming spherical symmetry, this temperature can be directly related to the total cluster mass profile (Böhringer & Werner, 2010). These however are not always valid assumptions as shall be discussed later.

Gravitational lensing Due to the large gravitational field exerted by galaxy cluster light passing in its vicinity is deflected. This lensing effect acts to create multiple images of background sources or even gravitational light arcs, as well as to systematically distort the background field. Naturally this distortion depends on the mass of the cluster, and through detailed analysis of the received image the cluster mass may be inferred (see Bartelmann (2010) for a thorough review). The mass received is however in terms of surface density, and the 3D distribution of matter has to be modelled, which is not always an easy task. It has been shown that the inferred 3D distribution is dependant of the line of sight through the structure (Clowe et al., 2004).

Sunyaev-Zel'dovich effect The photons of the cosmic microwave background travel along virtually un-

perturbed paths since the surface of last scattering. If however they happen to travel through a galaxy cluster they may interact with the hot gas of the cluster, yielding a net positive energy contribution to the photon. This in turn makes the cosmic microwave background appear hotter in this direction, and this temperature increase is related to the cluster mass. This is one of the most promising methods for mass estimation of galaxy clusters for several reasons, the perhaps most important one being that it is redshift independent. Therefore it can probe clusters at high redshifts relative to other techniques. Also it provides a very simple linear measure of column mass, and in this sense it is a relatively unambiguous signal. For more information see Carlstrom et al. (2002).

1.3 Aspherical clusters and thesis objectives

The virial theorem and Jeans equation masses are examples of dynamical methods of mass estimation. Both are faced with assumptions of equilibrium and more importantly sphericity, as the limited observable 3D phase-space of two angular coordinates and redshift in themselves are not sufficient. Naturally a range of different dynamical methods exist, each with their assumptions for the system under consideration to account for the limited observational information (Old et al., 2014). Common for most of them is that they assume spherical conditions.

There is a large body of evidence suggesting that galaxy clusters in fact are highly aspherical. On the observational side, the non-circular signals received through the available observational channels comprise density maps derived from the optical, surface brightness from X-ray, Sunyaev Zel'dovich pressure maps, lensing signals and more, summarized by Limousin et al. (2013). As an example, an X-ray map of Abell cluster 2597 is displayed in the right side of Fig. 1.2, as obtained from Limousin et al. (2013), showing clear aspherical features reasonably well fit by an ellipsoidal model. Furthermore, N -body simulations also show strong triaxiality of galaxy clusters with axial ratios on the order of 0.6 and with a preferentially prolate structure (Allgood et al., 2006). The anisotropy is present not only spatially, but also the velocity component of galaxy clusters shows clear anisotropy in observations (Wojtak, 2013).

The focus of the current work is on the effect of cluster asphericity on dynamical mass estimates. We probe this using the 'caustic technique of mass estimation' (Diaferio, 1999), which is extensively used to obtain dynamical masses (Biviano & Girardi, 2003; Rines & Diaferio, 2006; Geller et al., 2013; Rines et al., 2013). The technique is discussed in depth in the next chapter, however it works by estimating the escape velocity profile of a system of galaxies as a function of radius, and relates it to the potential and thus the mass profile of the system. As many of the techniques discussed above, it assumes spherical symmetry. The method does not rely on assumptions of dynamical equilibrium beyond the virial radius, and as such it can be used to probe cluster mass at large radii. Therefore it also allows for the possibility of probing asphericity effects radii beyond the virial radius. We aim to relax the spherical conditions to a triaxial model of galaxy clusters, as well as consider the possible effects of surrounding large scale structure in the shape of filaments, both which is expected to modulate the resulting dynamical mass.

The following chapter is organised as follows. Section 2.1 describes the treatment of data from an N -body dark matter particle simulation, and of selected halos within it. Section 2.2 describes the rotation and stacking of the clusters in ellipsoidal, filamentary and spherical stacks. Section 2.3 outlines the theory of the caustic technique for mass estimation of galaxy clusters. Section 2.4 presents the caustic mass estimates of the stacks as obtained by using different lines of sight, and Section 2.5 discusses how this works as a bias in mass estimation. Section 2.6 sums up the conclusions of the work done in this thesis, and Section 2.7 contains a brief outlook on potential future work.

Chapter 2

Asphericity and the caustic technique

The following chapter contains the description and analysis of caustic mass estimates on aspherical mock data from N -body simulations. It is largely identical to an article submitted to Monthly Notices of the Royal Astronomical Society based on the work made for this thesis. The article can be found on-line in its submitted form at <http://arxiv.org/abs/1405.0284>. Co-author statements from the two co-authors DARK Fellow Radek Wojtak and Assoc Prof Steen H. Hansen can be found in the back of the thesis.

2.1 Simulations and mock catalogues

The caustic technique of mass estimation takes as input the projected phase-space data of an observed galaxy cluster, i.e. the projected sky positions and line of sight velocities of its member galaxies. In order to apply and evaluate the performance of the caustic technique in spatially isotropic and anisotropic settings we set out to compile a range of mock phase-space diagrams of simulated galaxy clusters. We assume that realistic representations of phase-space diagrams of clusters can be obtained by considering just dark matter particles from N -body simulations. The particle data were obtained from the Bolshoi simulation¹, which simulates 2048^3 dark matter particles, each with a mass of $1.35 \times 10^8 h^{-1} M_{\odot}$ (Klypin et al., 2011). The simulation evolves from redshift $z = 80$ inside a box volume of side length $250 h^{-1} \text{Mpc}$ and uses cosmological parameters consistent with measurements based on the WMAP five-year data release (Komatsu et al., 2009) and the abundance of optical clusters from the Sloan Digital Sky Survey (Roza et al., 2010), $\Omega_m = 0.27$, $\Omega_{\Lambda} = 0.73$, $\sigma_8 = 0.82$ and $h = 0.7$ such that $H_0 = 100 h \text{ km s}^{-1} \text{Mpc}^{-1} = 70 \text{ km s}^{-1} \text{Mpc}^{-1}$.

We construct the phase-space diagrams by using two sets of data from the Bolshoi simulation at redshift $z = 0$ in conjunction, namely a location and velocity subset of 8.6×10^6 randomly drawn dark matter particles, along with a Bound Density Maximum (BDM) halo catalogue also obtained from the Multidark database, which lets halos extend up to an overdensity limit of $360 \rho_{crit}$, where ρ_{crit} is the critical density. Throughout, we shall refer to the former dataset when mentioning particles, and the latter when mentioning halos. For each halo in the catalogue all particles were assigned an additional radial Hubble flow velocity $v_h = 100 h r \text{ km s}^{-1} \text{Mpc}^{-1}$ according to their 3-dimensional distance r to the halo center. We choose to use the exact halo centers of the BDM catalogue here and throughout our analysis in order to provide optimal conditions for the application of caustic technique. To ensure comparable proportions of the halos, the positions of their member particles were normalized by the virial radius R_v and their velocities by the virial velocity $V_v = \sqrt{GM_v/R_v}$, where M_v is the virial mass. All of these quantities along with the halo center locations are provided in the BDM halo catalogue. Clusters were chosen within two mass bins, namely in the range of $M_v \in [1, 2] \times 10^{14} h^{-1} M_{\odot}$, which yielded 230 distinct halos in the catalogue, and $M_v > 2 \times 10^{14} h^{-1} M_{\odot}$ which yielded 101 distinct halos in the catalogue. The two shall throughout be referred to as the 'low mass bin' and the 'high mass bin' respectively.

¹The simulation is publicly available through the Multi Dark database (<http://www.multidark.org>). See Riebe et al. (2011) for details of the database.

2.2 Stacking the data

Two big sources of spatial anisotropy in clusters stems from elongation of the clusters themselves and surrounding large scale structure i.e. filaments, walls and voids. In order to isolate these morphological features for further analysis the halos from each mass bin were arranged concentrically in three separate stacks. For each stack all halos and their particles were rotated individually to align and isolate the geometric features of elongation and filamentary structure. This yielded for each mass bin:

- An *ellipsoidal stack* where halos were modelled as ellipsoidal structures and rotated so that the three principal axes of each halo were aligned
- A *filamentary stack* that aligned the direction of largest filament associated with each halo
- A *spherical stack* for reference with arbitrary orientation of each halo

The three configurations made it possible to choose any line of sight through the anisotropic stacks and compare mass estimates from caustics with those of the *spherical stack*. Because the stacks differ only in orientation of individual halos, they have the same true cumulative mass profile $M(< r)$. Therefore any difference in caustic mass estimation between the *ellipsoidal* or *filamentary stack* and the *spherical stack* expresses an anisotropy bias in the caustic method of mass estimation.

2.2.1 Ellipsoidal geometry and alignment

To create a smooth halo with clearly pronounced triaxiality and little interference from cluster substructure, ongoing merging or large scale structure, each of the halos were rotated according to their directions of elongation and placed in a stack. As a measure of elongation and orientation we invoked an ellipsoidal model by considering the shape tensor of each halo. Its three eigenvalues λ_i define the principal axes of the ellipsoid, and its eigenvectors define their orientation. For each halo the shape tensor S_{jk} (see e.g. Zemp et al. (2011)) can be obtained by summing over its N member particles within some radius:

$$S_{jk} = \sum_{i=1}^N (x_j)_i (x_k)_i. \quad (2.1)$$

Here x_j and x_k are the j 'th and k 'th components of the 3-dimensional position vector of the i 'th particle. We use particles within R_v to avoid interference from any nearby large-scale structure. The eigenvalues λ_a , λ_b and λ_c of S_{jk} then give the principal axes of the ellipsoid: $a = (\lambda_a)^{1/2}$, $b = (\lambda_b)^{1/2}$ and $c = (\lambda_c)^{1/2}$. The eigenvalues are ranked so that $a \geq b \geq c$. Their corresponding eigenvectors dictate the direction of each principal axis. The three semi-axes a , b and c of each cluster were aligned with the x -, y - and z -axis respectively. This configuration is sketched in the top part of Fig. 2.1, and it shall be referred to as an *ellipsoidal stack*.

For each of the halos, the triaxiality parameter T (Franx et al., 1991) is defined as

$$T = \frac{a^2 - b^2}{a^2 - c^2}. \quad (2.2)$$

Clusters with $T = 0$ are purely oblate, those with $T = 1$ are purely prolate. The triaxiality parameter will assist in dividing the clusters from each mass bin into ellipsoidal substacks binned according to T . This allows for an examination of the properties of predominantly oblate or prolate clusters. After stacking all halos in each mass bin the shape tensor was calculated within R_v for the stacks as a whole, yielding $b/a = 0.78$, $c/a = 0.65$ and $T = 0.69$ for the low mass bin, and $b/a = 0.76$, $c/a = 0.63$ and $T = 0.70$ for the high mass bin. Consequently this is a significantly aspherical prolate configuration for both mass bins. These numbers are also summarized in the 'Triaxiality' columns of Table 2.1.

2.2.2 Filament geometry and alignment

Filamentary structure may manifests itself as not necessarily straight strings of material between galaxy clusters. As a simple approach to create a smooth halo with a pronounced filament associated with it, we

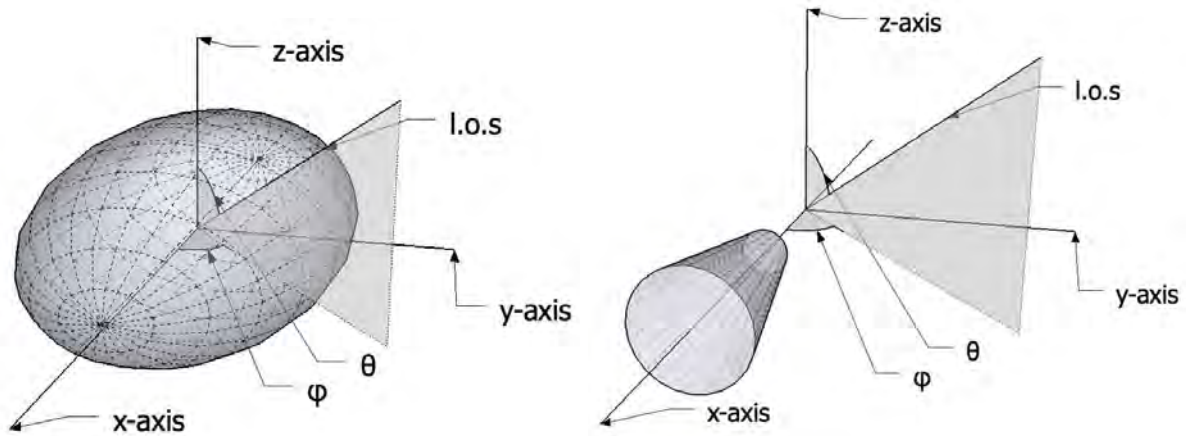


Figure 2.1: *Top*: Sketch showing the geometry of an *ellipsoidal stack*. Note how the ellipsoid has its longest major axis a along the x -axis, the shorter b along y and the shortest c along the z -axis. *Bottom*: Sketch showing the geometry of a filamentary stack. Notice the placement of the 30° cone frustum (filament) along the positive x -axis. The 'l.o.s.' arrow indicates the line of sight. Note that both figures are not to scale.

rotate each individual halo such that the largest filament associated with each halo (if any) is aligned with the positive x -axis. As a measure of filamentary structure the direction of highest particle number density as seen from the center of the halo was used. Particles between $1 R_v$ and $5 R_v$ were examined for each halo. The direction of maximal number density within a cone frustum of opening angle 30° was located. The particles from each halo were again placed concentrically in a stack, and rotated such that the maximal density direction was aligned with the positive x -axis. In this way the stack puts emphasis on surrounding filamentary structure. Because of the axisymmetric geometry of the cone frustum there are no preferred directions within the plane orthogonal to the filament, and consequently two random (orthogonal) directions were chosen within this plane for the y - and z -axis for each halo. This configuration is sketched in the bottom part of Fig. 2.1, and it shall be referred to as a *filamentary stack*. Note that only the filament frustum and not the core of the cluster is sketched in this figure, even though naturally still present. Because the stack is oriented after surrounding filaments, we expect the inner parts of it to be fairly spherical, although some alignment of ellipsoidal clusters principal axis and filaments have been reported (Hahn et al., 2007; Libeskind et al., 2013). Using a cone frustum as a geometric model of filaments in a stack will produce a very straight 'filament', which is true for some but not necessarily all individual clusters (Colberg et al., 2005). After stacking all halos according to their filamentary structure, the shape tensor for stack particles within R_v had $b/a = 0.89$, $c/a = 0.86$ and $T = 0.81$ for the low mass bin, and $b/a = 0.88$, $c/a = 0.85$ and $T = 0.81$ for the high mass bin. This configuration is much more spherical (within R_v) than that of the *ellipsoidal stack*, though some triaxiality is still present.

2.2.3 Spherical reference geometry

When testing for effects of anisotropy it is good to have an ideal spherical configuration as a reference point. To create a spherically symmetric halo, the individual halos in each mass bin were all superposed 10 times each in a third stack, with a new random rotation for each superposition. This yielded a highly spherical configuration, where triaxiality of clusters and filamentary structure was smoothed out on average. It shall be referred to as a *spherical stack*. With these three stack types in hand it is possible to investigate ellipsoidal cluster properties along different lines of sight using the spherical cluster properties as reference. The shape tensor for particles within R_v for this stack yielded $b/a = 1.00$ and $c/a = 0.99$ in the low mass bin and $b/a = 0.98$ and $c/a = 0.97$ for the high mass bin. Both are thus very close to a spherical distribution, in which case T is undefined.

2.3 The caustic technique

The escape velocity of a spherical gravitationally bound system of particles relates to its gravitational potential through

$$v_{esc}^2(r) = -2\Phi(r), \quad (2.3)$$

where r indicates the 3-dimensional distance to the center of the system. Since the potential is a non-decreasing function of r , one would expect to find fast moving objects closer to the cluster center, and gradually slower objects further out, with the maximally observed velocity defined by $v_{esc}(r)$.

Following the work of Diaferio (1999) we conduct an analysis of our stacked cluster particle data using the now standard caustic technique for mass estimation of galaxy clusters. The idea of the caustic procedure is to locate the amplitude of a caustic envelope which encloses bound particles placement in the projected (R - v) phase-space, and relate it to the escape velocity. Here, the observables R and v indicate the projected distance to the cluster center and the line of sight velocity respectively. The escape velocity profile relates directly to the potential which may then be integrated to find the contained mass profile of the cluster. To do so, one must assume sphericity. Note that the following sections relies heavily on derivations presented in Diaferio (1999), Serra et al. (2011) and Gifford et al. (2013).

2.3.1 Phase space density distribution

Different authors take slightly different approaches to determining the actual caustic amplitude from a set (R, v) of observed particles in projection. The usual approach involves estimating the underlying density distribution $f(R, v)$ by using each particle as a tracer in a kernel density distribution estimation. Let (R, v) describe any position in the projected (R - v) phase space, and let (R_i, v_i) describe the location of the i 'th particle tracer. We estimate the local density distribution at (R, v) by summing over all N particle tracers in our stack:

$$f(R, v) = \frac{1}{N} \sum_{i=1}^N \frac{1}{h_R h_v} K\left(\frac{R - R_i}{h_R}, \frac{v - v_i}{h_v}\right). \quad (2.4)$$

Here, h_R and h_v control the width of the kernel smoothing in the R and v directions respectively. Different forms of the kernel K will naturally yield different $f(R, v)$. Diaferio (1999) uses an adaptive kernel, whereas Gifford et al. (2013) use a Gaussian type kernel, which they argue introduces no significant error to the distribution estimate. We shall adapt the latter Gaussian kernel, which takes the form:

$$K(x_R, x_v) = \frac{1}{2\pi h_R h_v} \exp\left[-\frac{(x_R^2 + x_v^2)}{2}\right]. \quad (2.5)$$

We set $h_R = N^{-\frac{1}{6}}\sigma_R$ and $h_v = N^{-\frac{1}{6}}\sigma_v$ as the rule-of-thumb optimal size of the kernel, where σ_R and σ_v are the dispersions in the R - and v -direction respectively. For more information on these choices see statistical work by Silverman (1986), and cosmological work by Pisani (1993). The next step is to associate contours of constant $f(R, v) = \kappa$ with potential caustic amplitudes $\mathcal{A}_\kappa(R)$. A contour of $f(R, v)$ is going to appear more or less symmetrically around $v = 0$, and as such we chose for any R the minimum of the lower and the upper contour. The caustic amplitude at projected radius R is related to the escape velocity of the cluster by

$$\langle v_{esc}^2 \rangle_{R, \kappa} = \int_0^R \mathcal{A}_\kappa^2(r) \phi(r) dr / \int_0^R \phi(r) dr, \quad (2.6)$$

where $\phi(r) = \int f(r, v) dv$. The caustic amplitude $\mathcal{A}(r)$ is then chosen as the $f(r, v) = \kappa$ that minimizes

$$M(\kappa, R) = \left| \langle v_{esc}^2 \rangle_{R, \kappa} - 4 \langle v^2 \rangle_R \right|^2 \quad (2.7)$$

within the virial radius by setting $R = R_v$. For more information on this minimization see Gifford & Miller (2013). For $\langle v^2 \rangle_R$ we use the mass-weighted mean line of sight velocity dispersion inside $R = R_v$. When observing naturally R_v is not known a priori, and therefore an iterative scheme must be applied. An initial guess of R_v results in a caustic mass M_v , which converts to a new virial radius $\propto M_v^{1/3}$, with which the

caustic technique can be re-applied iteratively until convergence on the final caustic amplitude and observed virial radius $R_{v,obs}$. We choose an initial guess of $1 R_v$. Finally, we limit the caustic amplitude such that if $d \ln \mathcal{A} / d \ln r > \zeta$ we impose a new value for \mathcal{A} such that $d \ln \mathcal{A} / d \ln r = \zeta$. Following Serra et al. (2011) we choose $\zeta = 2$, to only cap the very rapid and non-physical increases in the escape velocity, although some authors have chosen lower values (Diaferio, 1999; Lemze et al., 2013). This yields a final caustic amplitude $\mathcal{A}(r)$, which will give the caustic mass profile in the next section.

2.3.2 Caustic amplitude and gravitational potential

With a measure of the caustic amplitude in hand, the usual approach is to relate it to the potential profile of the system. Diaferio (1999), Serra et al. (2011) and Gifford et al. (2013) implement some form of the equation

$$-2\Phi(r) = g(\beta)\mathcal{A}^2(r), \quad (2.8)$$

where $g(\beta) = \frac{3-2\beta}{1-\beta}$ and $\beta(r) = 1 - \langle v_\theta^2 + v_\phi^2 \rangle / 2 \langle v_r^2 \rangle$ is the velocity anisotropy parameter. Here v_θ , v_ϕ and v_r are the longitudinal, azimuthal and radial components of the 3-dimensional velocity, and brackets indicate the average over velocities in the volume d^3r at position r . We write the infinitesimal mass element for a sphere of density $\rho(r)$ in the form

$$G dm = -2\Phi(r)\mathcal{F}(r)dr, \quad (2.9)$$

where $\mathcal{F}(r) = -2\pi G\rho(r)r^2/\Phi(r)$. Using equation (2.8) in the above and integrating we get the cumulative mass profile as a function on $\mathcal{A}(r)$, $\mathcal{F}(r)$ and $g(r)$:

$$GM(< R) = \int_0^R \mathcal{F}(r)g(r)\mathcal{A}^2(r)dr. \quad (2.10)$$

Diaferio (1999) argues that the product $\mathcal{F}_\beta = \mathcal{F}(r)g(r)$ varies slowly with r , and can be taken as constant, which finally relates the caustic amplitude directly to the cumulative mass profile as

$$GM(< R) = \mathcal{F}_\beta \int_0^R \mathcal{A}^2(r)dr. \quad (2.11)$$

The choice of \mathcal{F}_β varies for different authors. We use a value of $\mathcal{F}_\beta = 0.58$ which is in line with previous work (e.g. Diaferio, 1999; Serra et al., 2011; Gifford et al., 2013). It is slightly low compared to Fig. 7 of (Biviano & Girardi, 2003), however in good agreement with Fig. 11 of (Biviano et al., 2013) and Fig. 9 of (Lemze et al., 2009). Using this value we recover the true cumulative mass profiles using the *spherical stacks* excellently up to within $2 R_v$, as shall be discussed in later sections of this paper (see bottom of Fig. 2.3). In any case when considering relative cumulative mass profiles this factor cancels itself out.

In short the distribution of particles in projected phase space as obtained by equation (2.4), and the velocity dispersion entering in equation (2.7) work together to define and select the caustic amplitude. It is precisely the interplay between these two mechanisms that spatial anisotropy is expected to affect, such that the inferred mass profile from aspherical clusters obtained with equation (2.11) might deviate from the spherical case. An overview of the computational process from particle data to caustic amplitudes can be seen in Fig. 3 of the appendix.

2.4 Results

To quantify how the geometry of clusters affects the amplitude selected by the caustic technique for different projections, both the *spherical*, *ellipsoidal* and *filamentary stack* were projected using varying lines of sight for both mass bins under consideration. Fig. 2.2 shows the density distribution $f(R, v)$ as calculated by the kernel density estimation technique described in Section 2.3.1. The distribution is calculated from the low mass bin *spherical stack* for an example choice of line of sight at $(\theta, \phi) = (90^\circ, 0^\circ)$. The black isodensity contours show the classical trumpet shape along which we expect the caustic amplitude to lie. The white dashed lines on the plot shows the actual caustic amplitude for this distribution as found by the caustic method described above. The widening velocity dispersion at $> 2 R_v$ is a natural consequence of the added

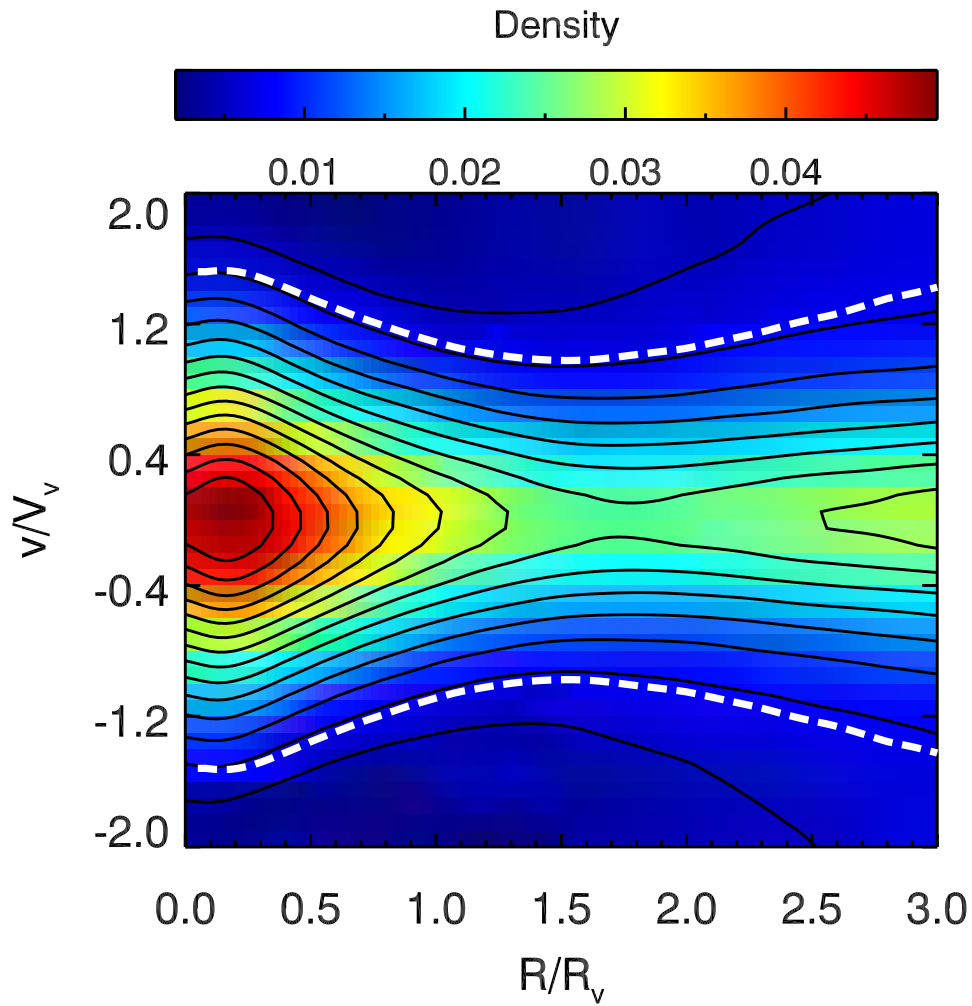


Figure 2.2: Projected density distribution of DM particles of the 230 clusters from the low mass bin *spherical stack* as obtained by the Gaussian kernel. Black lines indicate isodensity contours, and the white dashed lines indicates caustic amplitude selected by the caustic technique.

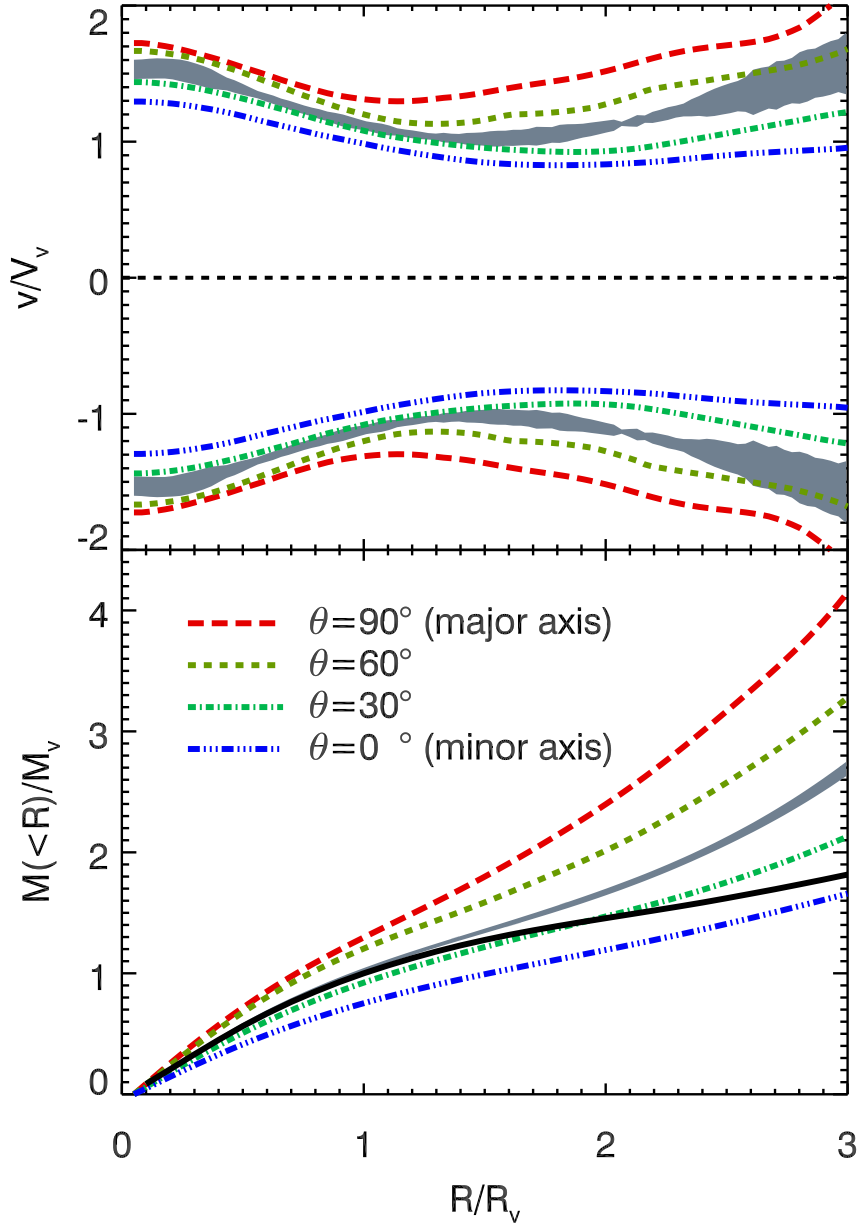


Figure 2.3: *Top*: Caustic amplitudes for the low mass bin *ellipsoidal stack* using 4 different lines of sight with $\phi = 0^\circ$ and θ as indicated by the legend. This corresponds to moving gradually from a line of sight along the major axis of the stack towards a line of sight along the minor axis. The grey area shows two standard deviations of caustic amplitudes through the spherical stack, as obtained by integrating the grey area in the bottom panel of this figure (see below). *Bottom*: The resultant cumulative mass profiles as obtained by applying equation (2.11) to the amplitudes of the top plot. Grey area shows two standard deviations of 10,000 mass profiles from random lines of sight through the *spherical stack*. The solid black line shows the true mean mass profile of the 230 clusters as calculated from the full Bolshoi particle data set.

Hubble flow. We stress that this figure is very representative of the density distribution from any line of sight through the *spherical stacks*.

In the top panel of Fig. 2.3 the curves which are symmetric around $v = 0$ show caustic amplitudes found for the low mass bin *ellipsoidal stack* for 4 lines of sight with directions as indicated on the bottom panel. The outer red long dashed curves show the caustic amplitude found using a sight line along the semi-major axis of the stack, i.e. $(\theta, \phi) = (90^\circ, 0^\circ)$. The inner blue dash-dot-dot-dotted curves show the caustic amplitude found from a sight line along the semi-minor axis of the stack, i.e. $(\theta, \phi) = (0^\circ, 0^\circ)$. The two curves in between shows caustic amplitudes using sight lines $\theta = 60^\circ$ (green short dashed) and $\theta = 30^\circ$ (cyan dash-dot) (see legend in the bottom plot of Fig. 2.3). The bottom panel of Fig. 2.3 shows the cumulative mass profiles $M(< R)$ as obtained from the caustic amplitudes shown in the top panel combined with equation (2.11). The red long dashed, green short dashed, cyan dash-dotted and blue dash-dot-dot-dotted lines are thus from the low mass bin *ellipsoidal stack* with line of sight as indicated in the legend, keeping $\phi = 0^\circ$.

In order to gain a reference point for evaluating the anisotropic stacks, lines of sight were chosen to cover the half sphere of both the low and high mass bin *spherical stack* in a $15^\circ \times 15^\circ$ grid from $\theta \in [0^\circ, 90^\circ]$ and $\phi \in [-180^\circ, 180^\circ]$. The mean cumulative mass profile $M_s(< R)$ was then calculated for the spherical stacks. This was done by choosing 10,000 pairs of (θ, ϕ) randomly distributed on the sphere, interpolating the mass profiles from the $15^\circ \times 15^\circ$ grid to obtain 10,000 mass profiles, and then taking the average profile. $M_s(< R)$ and its 95.4% variability for the low mass stacks can be seen as the grey shaded area of Fig. 2.3 on the bottom. The black solid line shows the mean of the true cumulative mass profiles calculated from the full Bolshoi particle data set for each of the 230 clusters used in the three stacks. The caustic mass estimates of the *spherical stack* agrees well with the true mass profile until $2 R_v$, from where the mass is overestimated. We note that this is the case given $\mathcal{F}_\beta = 0.58$, which motivates our choice, however the overestimation of mass at large radii suggests that \mathcal{F}_β should be taken as a function of radius. As we (in line with previous work) assume a constant \mathcal{F}_β and furthermore consider only relative mass estimates, the actual value of \mathcal{F}_β becomes irrelevant. Through equation (2.11) the caustic amplitude obtained from $M_s(< R)$ and its 95.4% variability is shown in the top part of the same figure.

To fully map out the angular dependency of the mass estimates of the caustic technique on the anisotropic stacks, lines of sight were chosen in the same $15^\circ \times 15^\circ$ grid as above, covering the half sphere. From an ellipsoidal point of view, the four octants that span the half sphere are equivalent. Thus properties like position, velocity dispersion and inferred caustic mass for the four example lines of sight $(\theta, \phi) = \{(-165^\circ, 15^\circ), (-15^\circ, 15^\circ), (15^\circ, 15^\circ), (165^\circ, 15^\circ)\}$ should be symmetric in these octants. By using the chosen grid, the cumulative mass profiles $M_{\theta, \phi}(< R)$ for each octant were calculated, and the average octant was taken. The resulting profiles were normalized to the mean of the *spherical stack* $M_s(< R)$ (grey shaded area of Fig. 2.3 bottom). This way the normalized profiles express an intrinsic bias of the caustic method from spatial anisotropy, relative to the caustic mass profile inferred when the assumption of sphericity is perfectly valid.

The three top panels of Fig. 2.4 show the relative cumulative mass estimates at 1, 2 and 3 R_v for the average octant of the low mass bin *ellipsoidal stack*. The lower right corner of each panel at $(90^\circ, 0^\circ)$ represents the line of sight along the major axis. The upper right corner at $(90^\circ, 90^\circ)$ represents the intermediate axis and the entire left side at $\theta = 0^\circ$ represents the minor axis for any ϕ . The color of the figure shows the value of the cumulative mass at a given radius relative to the spherical mass estimate. Table 2 of the Appendix shows the numeric values for each set of angles. The bottom three panels of Fig. 2.4 shows the same as the top three but for the *filamentary stack*. The lower right corner of each panel represents the line of sight along the maximal density direction i.e. along the filament. The entire upper ($\phi = 90^\circ$) and left ($\theta = 0^\circ$) side represents lines of sight orthogonal to the filament. Table 3 of the Appendix shows the numeric values for each set of angles in each panel.

We stress that the masses displayed here (and throughout the paper) are evaluated at multiples of the true virial radius R_v , not the observed virial radii $R_{v, obs}$ provided by the caustic method. Upon iteratively determining the caustic mass and caustic virial radius $R_{v, obs}$, the masses at 1, 2 and 3 $R_{v, obs}$ deviate from those displayed in this figure. As an example the data mass profiles of Fig. 2.4 are evaluated at $R_{v, obs}$ rather than R_v in Fig. 4 of the Appendix.

Fig. 2.5 also shows the angular dependency of the caustic mass estimates for the *ellipsoidal* and *filamentary stack* but for the high mass bin i.e. the same thing as Fig. 2.4 but for more massive clusters. Tables 4

Table 2.1: Values of triaxiality and mass estimates for the different stacks under consideration. The three 'Triaxiality' columns show the intermediate to major axis ratio b/a , the minor to major axis ratio c/a and the triaxiality parameter T for each of the stacks in questions for particles within R_v . The 'Mean mass' columns show the mean of 10,000 mass measurements obtained from 10,000 interpolations of each panel in Fig. 2.4 and Fig. 2.5 for 10,000 directions randomly distributed on the sphere. The 'Scatter in masses' columns show the scatter defined as the standard deviation of the 10,000 mass measurements. The 'Max/min mass' columns show the ratio of the maximum mass estimate to the minimum mass estimate for each panel in Fig. 2.4 and Fig. 2.5. All mass values are normalized by M_s .

Stack name	Triaxiality			Mean mass			Scatter in masses			Max/min mass		
	b/a	c/a	T	$1 R_v$	$2 R_v$	$3 R_v$	$1 R_v$	$2 R_v$	$3 R_v$	$1 R_v$	$2 R_v$	$3 R_v$
$[1, 2] \times 10^{14} h^{-1} M_\odot$												
Ellipsoidal Stack	0.78	0.65	0.69	1.02	1.05	1.06	0.14	0.19	0.27	1.72	1.95	2.44
Filamentary Stack	0.89	0.86	0.81	1.00	0.99	0.98	0.06	0.13	0.21	1.22	1.49	1.71
Spherical Stack	1.00	0.99	-	1.00	1.00	0.99	0.01	0.01	0.01	1.03	1.06	1.13
$\geq 2 \times 10^{14} h^{-1} M_\odot$												
Ellipsoidal Stack	0.76	0.63	0.70	1.03	1.05	1.07	1.19	0.23	0.34	2.06	2.22	2.95
Filamentary Stack	0.88	0.85	0.81	1.01	1.00	1.00	0.07	0.09	0.14	1.21	1.32	1.38
Spherical Stack	0.98	0.97	-	1.00	1.00	0.99	0.01	0.01	0.02	1.04	1.06	1.11

and 5 of the Appendix show the numerical values for each set of angles in each panel.

Table 2.1 shows values derived from the data displayed in Fig. 2.4 and 2.5. The 'Mean mass' columns were generated in the same way as the spherical mean mass profiles $M_s(< R)$ by choosing 10,000 sets of (θ, ϕ) randomly distributed on the sphere, and then interpolating the mass estimates shown in Fig. 2.4 and 2.5. The mean of these 10,000 mass estimates are then the 'Mean mass' at a given radius, but normalized to $M_s(< R)$. The 'Scatter in masses' columns show the 68.3% standard deviation of the 10,000 mass estimates for each stack and radius. Finally the 'Max/min mass' columns show for the spherical stack the maximum mass estimated relative to the minimum mass estimate at 1, 2 and $3 R_v$. For the *ellipsoidal stack* it shows the major axis mass estimate relative to the minor axis mass estimate for each of the top panels in Fig. 2.4 and 2.5. For the *filamentary stack* the columns show the mean of the mass estimates at $(\theta, \phi) = \{(75^\circ, 0^\circ), (75^\circ, 15^\circ), (90^\circ, 15^\circ)\}$ relative to the mean of the seven mass estimates orthogonal to the filament at $\phi = 90^\circ$. This represents the largest mass estimate relative to the lowest, taking into account the symmetry of the stack because the biggest mass overestimate appears when the line of sight is tilted slightly at $\sim 15^\circ$ to the filament axis. This will be discussed in detail in the next section.

2.5 Discussion

The increased statistics of the two *spherical stacks* allows for a very consistent estimate of their true caustic amplitudes and masses, regardless of the choice of line of sight. Both the *spherical*, *ellipsoidal* and *filamentary stacks* consist of the same number of clusters within each mass bin, and thus have the same true cumulative mass profile. Any cumulative mass profiles found in the *ellipsoidal* and *filamentary stacks* that differ from those of the *spherical stacks* therefore result from a spatial anisotropy bias in the caustic technique. Fig. 2.3 shows clearly how the mass profiles from the caustic procedure can be affected by asphericity for the low mass bin: When observing the *ellipsoidal stack* along its most elongated direction (major axis at $(\theta, \phi) = (90^\circ, 0^\circ)$) the caustic amplitude and its subsequent mass estimate (red long dashed curves) are larger than for a spherical object of the same true mass (grey areas). By choosing lower θ for the line of sight and thereby making the cluster less elongated in these directions, the caustic amplitudes systematically drop in magnitude until they reach a minimum at $\theta = 0^\circ$ (blue dash-dot-dot-dotted curves), well below the mass estimate of the spherical

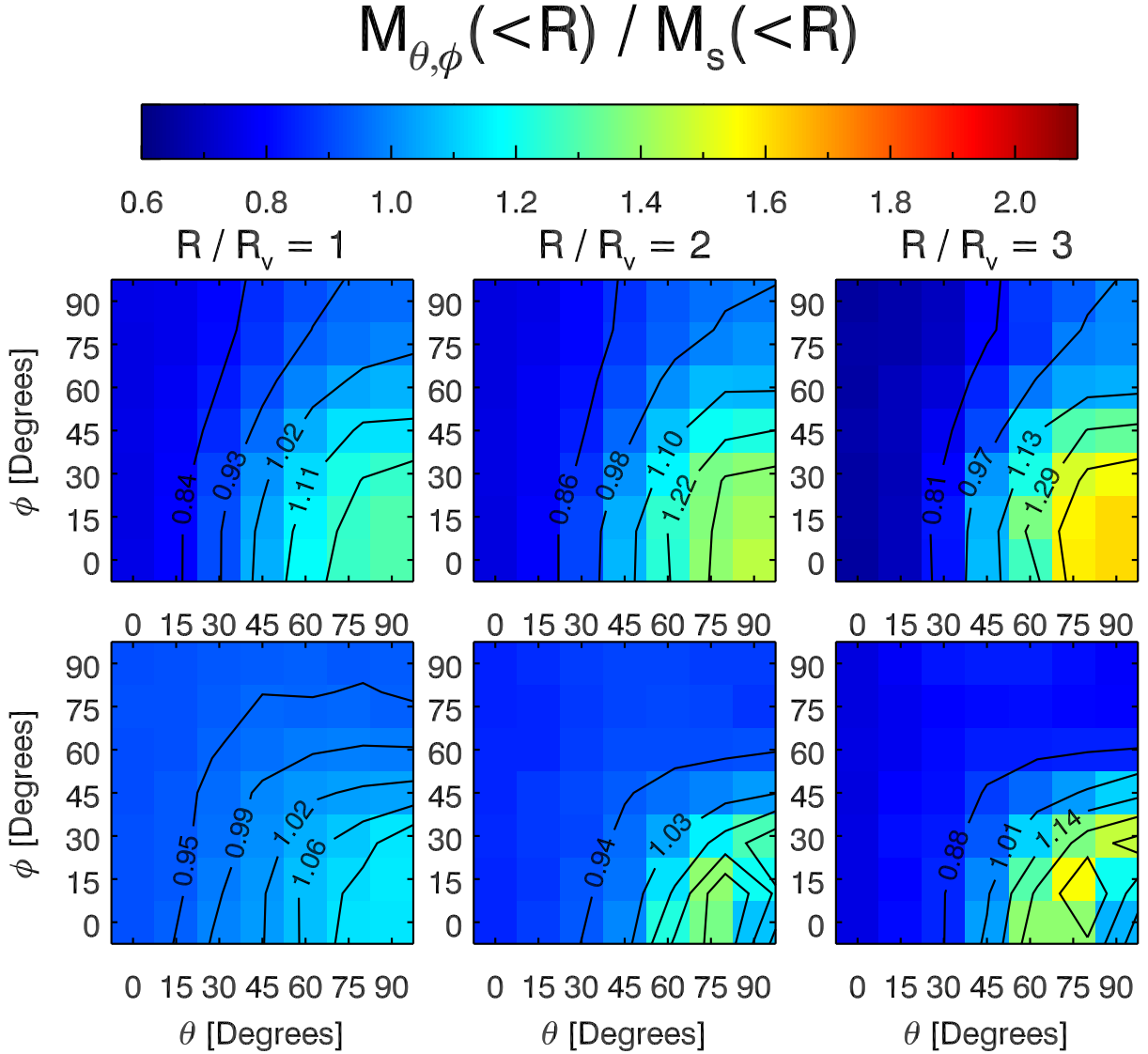


Figure 2.4: Effect of the cluster orientation on the mass estimate with the caustic method for the low mass bin i.e. $M_v \in [1, 2] \times 10^{14} h^{-1} M_\odot$. The panels show the mass estimates as a function of the orientation, relative to the mass M_s inferred from the *spherical stack*. The three columns show results for three choices of radii. The top row shows mass estimates for the *ellipsoidal stack* and the bottom row shows the same for the *filamentary stack*. θ and ϕ indicates the line of sight in question, defined for each stack in Fig. 2.1. For the top panels $(90^\circ, 0^\circ)$ represents the sight line along the major axis, $(90^\circ, 90^\circ)$ represents light line along minor axis and entire left side at $\theta = 0^\circ$ represents the minor axis for any ϕ . For the bottom panels $(90^\circ, 0^\circ)$ represents the sight line along the filament, and entire left side ($\theta = 0^\circ$ for any ϕ) and top ($\phi = 90^\circ$ for any θ) represent sight lines orthogonal to the filament. The color for any (θ, ϕ) indicates the value of the mass estimate as indicated on the linear colorbar. The lines in each panel show equally-spaced isodensity contours.

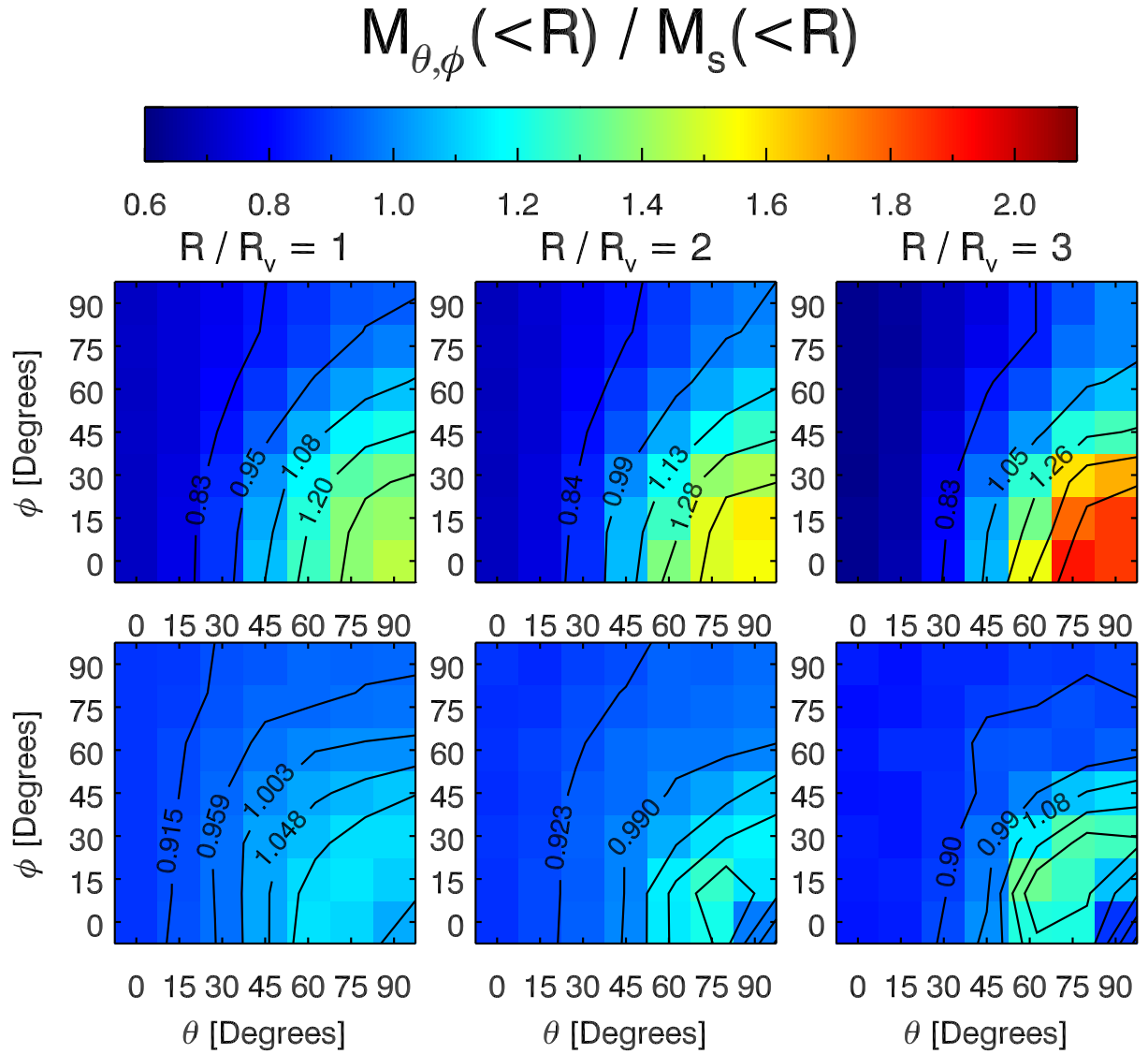


Figure 2.5: Same as Fig. 2.4 but for the high mass bin i.e. $M_v \geq 2 \times 10^{14} h^{-1} M_\odot$.

object. Clearly the more an elongated object has its axis of most elongation along the line of sight, the larger cumulative mass the caustic procedure will find at any radius. Similarly, the closer its least elongated direction is to the line of sight, the smaller cumulative mass the caustic procedure will find.

2.5.1 Low mass bin

Focusing on the low mass bin, Fig. 2.4 shows the mass estimates at 1, 2 and $3 R_v$ for a line of sight at varying angles θ and ϕ for both the low mass bin *ellipsoidal* and *filamentary stack*. All mass estimates are normalized by the mean cumulative mass profile $M_s(< R)$ from the *spherical stack*. Consistent with expectations from Fig. 2.3 the largest deviations from spherical mass estimates in the *ellipsoidal stack* (top three panels) appears once the line of sight coincides with either the major $((\theta, \phi) = (90^\circ, 0^\circ))$ or the minor axis $(\theta = 0^\circ$ for any $\phi)$. The mass estimate along the intermediate axis $((\theta, \phi) = (90^\circ, 90^\circ))$ lies comfortably in between the two extremes and generally the mass estimates follow a smooth transition between the extremes of the three principal axes. Along the major axis the cumulative mass estimates are 1.30, 1.46 and 1.60 times larger than the spherical mass estimates at 1, 2 and $3 R_v$ respectively. Along the minor axis the cumulative mass estimates are a factor of 0.75, 0.74 and 0.66 lower than the spherical mass estimates at the same radii as before. Taking the ratio of the maximal mass estimate to the minimal mass estimate, this effect spans a factor of 1.72, 1.95 and 2.44 at 1, 2 and $3 R_v$ respectively, as noted in Table 2.1. Table 2.1 also lists the mean mass of 10,000 random direction interpolations of the three top panels, i.e. an estimate of the bias. For the *ellipsoidal stack* this is close to one at any of the measured radii, meaning that caustics used on ellipsoidal structure on average is unbiased relative to spherical cluster mass estimates. The standard deviation of the 10,000 random direction mass profiles relative to the spherical mass is also listed in Table 2.1. The listed values of 0.14 at $1 R_v$ and 0.27 at $3 R_v$ is in good agreement with the lower limits of Serra et al. (2011) and Gifford et al. (2013) who both estimated scatter for a variable number of member galaxies.

The *filamentary stacks* are different from the *ellipsoidal stacks* both by construction and in the resulting bias effect. Inspecting Fig. 2.4 for the low mass bin *filamentary stack* (bottom three panels) one sees a general increase in mass at angles close to $(\theta, \phi) = (90^\circ, 0^\circ)$ which represents a line of sight directly along the filament, and a general decrease in mass at line of sight orthogonal to the filament. Upon closer inspection of the maximal mass estimate in the lower right corners of the three panels, one notes that the maximum occurs as the line of sight is slightly tilted to $\sim 15^\circ$ with respect to the filament axis i.e. at $(\theta, \phi) = \{(75^\circ, 0^\circ), (75^\circ, 15^\circ), (90^\circ, 15^\circ)\}$. The mean of the 3 mass estimates at this tilt is a factor of 1.13, 1.31 and 1.38 larger than $M_s(< R)$ at 1, 2 and $3 R_v$ respectively. Whereas the filament direction was chosen uniquely as the maximal density direction, the two other directions were selected at random within the plane orthogonal to the filament. As such, a different realization of the stack would yield a different orientation of all the clusters two unit vectors within the orthogonal plane. Indeed slight differences were observed for different realizations of the stack, and the column represented by $\phi = 90$ represents 7 lines of sight within the plane orthogonal to the filament, and thus we would expect the same mass estimate. We therefore take the average of these seven values and obtain a mass estimate of the *filamentary stack* lower by factor of 0.93, 0.88 and 0.80 at 1, 2 and $3 R_v$ when observing orthogonal to the line of sight. This yields a maximum-to-minimum ratio of 1.22, 1.49 and 1.71 at these radii. As such, the effect of filamentary anisotropy is slightly smaller than, yet comparable to the effect of elongation of the central structure for the low mass bin. From Table 2.1 we see that the mean mass is slightly smaller than the spherical case, similarly the scatter in masses is slightly smaller for the case of filaments than for the case of elongation.

In order to explain the shift in maximum of mass estimates for the low mass *filamentary stack* of $\sim 15^\circ$ we remind that the *filamentary stack* is constructed by orienting individual structures after the maximal density direction as found within a search cone frustum spanning 30° in angle between 1 and $5 R_v$ (see Section 2.2.2). As can be seen in e.g. Cuesta et al. (2008), the radial velocity component of particles in a galaxy cluster is zero on average up to $\sim 1.5 R_v$. Further out between $\sim 1.5 R_v$ and $3.5 R_v$ the radial velocity tends to be negative in a zone of infall towards the cluster. Still further out the Hubble expansion takes over and the radial velocity becomes positive and increases with radius (see Fig. 4 of Cuesta et al. (2008)). The cone frustum covers roughly equally much of the infall zone and the hubbe expansion zone, and as such we expect the particles within the filament to appear more or less symmetrically around $v = 0$ in $(R-v)$ -phase space. Fig. 2.6 shows the phase space density distribution for 4 lines of sight through the low mass bin *filamentary stack*. The grey diamonds and white stars show 400 particles drawn from either

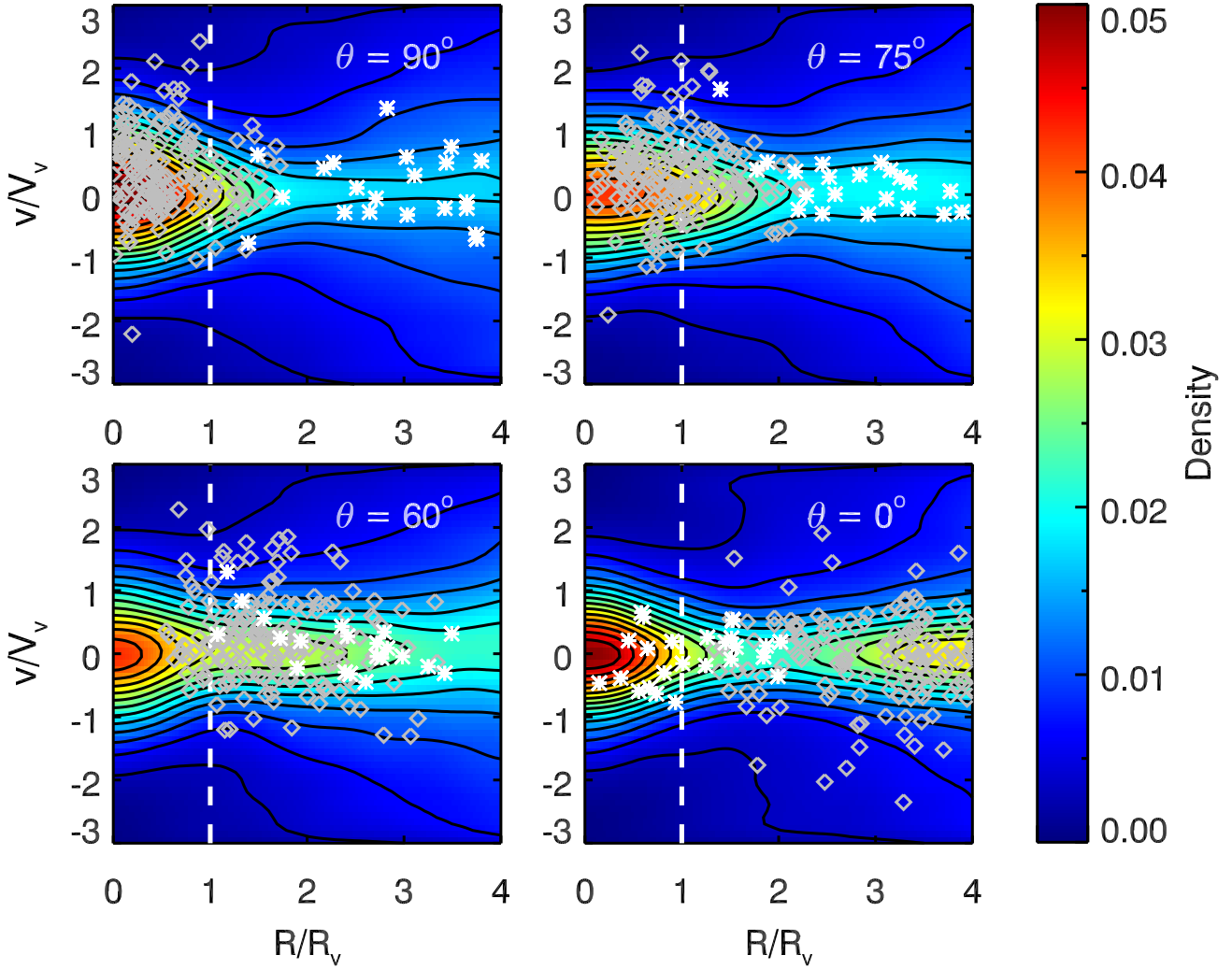


Figure 2.6: Location of filament particles in (R, v) phase-space using different projections. The data is from the low mass bin *filamentary stack* (i.e. $M_v \in [1, 2] \times 10^{14} h^{-1} M_\odot$) obtained by a constant $\phi = 0^\circ$ and a θ as indicated in white in each panel. $\theta = 90^\circ$ indicates a sight line directly along the filament, and $\theta = 0^\circ$ indicates the sight line orthogonal to the filament. The coloured contours represent the density obtained by the kernel density estimation method. The grey diamonds and white stars are projections of a total of 400 randomly drawn particles from within the filament frustum (grey diamonds) or a similar volume orthogonal to the filament (white stars). The white dashed line marks the location of R_v . Note that some points may fall outside the plotting range.

within the cone frustum i.e. the core of the filament, or in a similar volume along the positive y -axis. Points inside the filament frustum are indicated as grey diamonds, those in the orthogonal volume are shown as white stars. The majority of the points are located within the filament pr. construction of the stack, and consequently there are many more diamonds than stars on all figures. The important thing to note is where filament particles place themselves in projection for a given line of sight. When viewing the stack along its filament at $\theta = 90^\circ$ most of the filament particles project well within R_v . Here they add some, but not much to the overall mean velocity dispersion which is used to calibrate the derived caustic amplitude (see equation (2.7)). When viewing the filament at a slight angle with $\theta = 75^\circ$ the filament particles spreads over the entire inner part of the cluster in projection, acting to perturb the isodensity contours and increase the velocity dispersion. This in turn results in an overall larger caustic amplitude and thus larger mass estimate. As the line of sight is shifted even more to $\theta = 60^\circ$, the filament particles have left the inner parts of the cluster in projection, and thus affects the caustic amplitude chosen by equation (2.7) less. Finally at line of sight orthogonal to the filament at $\theta = 0^\circ$ all the filament particles are projected to high radii, and interfere only with the mass estimate at these radii.

Fig. 4 of the Appendix shows the same as Fig. 2.4 however with masses evaluated at observed $R_{v,obs}$ rather than the true R_v . The caustic method systematically overestimates the virial radius with line of sight along the semi-major axis, and underestimates it along the semi-minor axis. Thus the mass evaluated at the observed radii will depend on line of sight in the same way as in Fig 2.4 but with a slightly larger spread as can be seen in the resemblance of the two figures.

2.5.2 High mass bin

Upon comparing Fig. 2.4 for the low mass bin with Fig. 2.5 for the high mass bin, one notices some resemblance. For the high mass bin *ellipsoidal stack* represented in the three top panels of Fig. 2.5 there is still a systematic effect of overestimation of mass along the major axis and an underestimation along the minor axis, with the intermediate axis mass estimate lying in between. The effect is even larger for the high mass bin than low mass bin, with a major to minor axis mass ratio of 2.06, 2.22 and 2.95 at 1, 2 and 3 R_v respectively. As can be seen in Table 2.1 the low and high mass *ellipsoidal stacks* are very similar in respect to triaxiality and elongation, so the larger caustic mass estimates may therefore result from differences in velocity distribution or differences in elongation evaluated from particles at $> R_v$. The 'Mean mass' columns of Table 2.1 show that elongation of the cluster imposes a $< 4\%$ systematic bias in the mean of mass profiles on average within R_v . The 'Scatter in masses' column shows the slightly higher scatter in comparison with the low mass bin, however still in line with expectations.

For the high mass *filamentary stack* shown in the three bottom panels of Fig. 2.5 there is still a maximum overestimation at a 15° tilt from line of sight along the filament. Where ellipsoidal effects caused a larger scatter in mass estimates for the high mass bin, the effect of filaments seems to be marginally reduced. As such the *filamentary stack* showed a maximum to minimum mass estimate ratio of only 1.21, 1.32 and 1.38 at 1, 2 and 3 R_v . Colberg et al. (2005) reports that the number of filaments associated with a cluster increases for increasing halo mass, which may act to smear out the contrast between line of sight along the filament, and line of sight across the filament in the stack. Furthermore a large cluster does not necessarily mean a large filament, and as such the heavier clusters are less affected by the filament.

2.5.3 Triaxiality

It is interesting to quantify whether the mass measurements shown in Fig. 2.4 and 2.5 for the *ellipsoidal stacks* depend on triaxiality, i.e. if the distribution of mass estimates in (θ, ϕ) -space looks different for mainly oblate or prolate clusters. By splitting the *ellipsoidal stacks* into substacks of the most prolate and the most oblate, we obtain an 'oblate' stack with $T = 0.31$ using the 40 most oblate clusters and a 'prolate' stack with $T = 0.89$ using the 40 most prolate clusters for the low mass bin. Similarly we make a 19 cluster oblate ($T = 0.34$) and prolate ($T = 0.89$) substack for the high mass bin. We perform the same angular gridded analysis of all substacks as for the full stacks. Fig. 2 of the Appendix shows the mass estimates of the low mass bin prolate (top panels) and oblate (bottom panels) substack relative to the mean mass profile $M_s(< R)$

of the *spherical stack*². Upon comparing the substacks of Fig. 2 to the *ellipsoidal stack* in the top panels of Fig. 2.4 one sees very little variation from the low mass bin *ellipsoidal stacks* to the oblate and prolate counterparts. Similarly the high mass bin shows little variation between the oblate and prolate substacks of Fig. 3 of the Appendix and the high mass bin *ellipsoidal stacks* in Fig. 2.5. For this sparse sample of galaxy clusters we therefore conclude oblateness and prolateness to affect mass estimation in more or less the same manner. Naturally by cutting the stack cluster population in half the statistics suffer, and the estimates of Fig. 2 and 3 should be considered less certain. All values for the prolate and oblate substacks are summarized in Table 1 of the Appendix.

2.6 Conclusion

We studied the bias in the mass estimate of galaxy clusters based on the caustic technique, resulting from orientation of clusters with respect to the line of sight. We analysed dark matter particle data from the Bolshoi N -body simulation for a set of 230 dark matter halos at $M_v \in [1, 2] \times 10^{14} h^{-1} M_\odot$ and a set of 101 dark matter halos at $M_v > 2 \times 10^{14} h^{-1} M_\odot$. Each of the halos were superposed concentrically in 3 separate stacks differing only by orientation of the individual halos: The *ellipsoidal stack* had each halo rotated such that the three principal axes from its shape tensor inside R_v were aligned with the x -, y - and z -axis. The *filamentary stack* had each halo oriented after the direction of maximal density inside a cone frustum of angle 30° between $1 R_v$ and $5 R_v$, such that they were all oriented along the positive x -axis. The *spherical stack* had all halos stacked with completely random orientation, were each halo was used 10 times with a new random orientation each time to increase sphericity of the stack. Using the now standard caustic technique for mass estimation of galaxy clusters we projected each of the stacks to a $15^\circ \times 15^\circ$ angular grid in both mass bins and estimated the apparent caustic amplitude and cumulative mass profile for all angles. When using the mass estimate of the *spherical stack* for the low mass bin we found a good correspondence with the true cumulative mass profiles when using $\mathcal{F}_\beta = 0.58$, as shown in Fig. 2.3. Using the *spherical stack* as reference for the idealized situation under which the caustic method can be applied, we saw that the caustic amplitudes varied systematically with line of sight in the *ellipsoidal stack*. Using a line of sight along the major axis, we found that the caustic mass estimate was overestimated by a factor of 1.30, 1.46 and 1.60 relative to the mean *spherical stack* mass estimate at 1, 2 and $3 R_v$ respectively. Similarly with a line of sight along the minor axis the mass was underestimated with a factor of 0.75, 0.74 and 0.66 at the same radii relative to the *spherical stack*. Taking the ratio of the maximal mass estimate to the minimal mass shows that the effect is as large as a factor of 1.72, 1.95 and 2.44 at 1, 2 and $3 R_v$ respectively. We found that on average the caustic mass estimates for the *ellipsoidal stack* were unbiased relative to the spherical stack on average. For the low mass bin *filamentary stack* the same analysis was performed and yielded an overestimation of cumulative mass of 1.13, 1.31 and 1.38 at 1, 2 and $3 R_v$ with line of sight slightly tilted to along the filament, and an underestimation by factor of 0.93, 0.88 and 0.80 at 1, 2 and $3 R_v$ when observing orthogonal to the filament. This gave a maximum to minimum ratio of 1.22, 1.49 and 1.71 at these radii, which very somewhat smaller than, but comparable to the ratios of the *ellipsoidal stack*. We investigated the fact that the largest mass overestimate occurred when the line of sight was tilted at a 15° angle to the filament. We traced this effect to the location of the filament particles in projection, which had a maximal influence on velocity dispersion and caustic isodensity contours at 15° as demonstrated in Fig. 2.6.

For the large of the two mass bins, the systematics of the effects were the same, but the magnitude different. The caustic masses were still overestimated along the major axis of the *ellipsoidal stack* and underestimated along the minor axis. This effect was however even larger for the high mass bin with a maximum mass to minimum mass ratio of 2.06, 2.22 and 2.95 at 1, 2 and $3 R_v$ respectively. On the other hand the *filamentary stack* showed a lower influence of filaments on larger clusters, spanning only a maximum to minimum mass ratio of 1.21, 1.32 and 1.38 at 1, 2 and $3 R_v$.

We found that the scatter in mass estimates due to ellipsoidal and filamentary anisotropy is in good agreement with the lower limits of Serra et al. (2011) and Gifford et al. (2013) who both estimated scatter in caustic mass for a variable number of member galaxies. Thus a significant portion of the scatter presented

²Note that $M_s(< R)$ is for the full *spherical stacks*, and as such may differ slightly from the true mass profile of the prolate and oblate substacks

in these references may be explained by anisotropic models in the form of ellipsoids, and to a lesser extent filaments.

To test the sensitivity of caustic mass estimates on oblate- and prolateness we considered substacks of the 40 most oblate and prolate halos of the low mass bin *ellipsoidal stack* as defined by T , and substacks of the 19 most oblate and prolate halos of the high mass bin *ellipsoidal stack*. We found no significant variation by comparing oblate to prolate mass estimates, or by comparing the oblate and prolate masses to the full *ellipsoidal stack*.

The mass estimates plotted in Fig. 2.4 and 2.5 can be used to correct caustic mass estimates when cluster orientation is known. The numerical values from these figures are available in Table 2, 3, 4 and 5 of the Appendix.

The caustic method of mass estimation performs well when the condition of cluster sphericity is met. If however spatial anisotropy is present in the form of cluster elongation or filamentary structure, the caustic masses are strongly dependent on the line of sight through the cluster. Even within the virial radius the mass estimates may vary by a factor of ~ 2 for heavy clusters, and as such great care should be taken when applying this method.

The reason why the caustic mass measurements depend on the cluster orientation with respect to the line of sight is the anisotropy of the spatial as well as velocity distribution of galaxies in clusters. Considering the velocity component, this means that the effect of asphericity on the measurement of cluster masses is expected to be a generic feature of all kinematic methods for the cluster mass determination, e.g. methods based on the virial theorem or the scaling relation between cluster mass and the line-of-sight velocity dispersion (Biviano et al., 2006; Saro et al., 2013), methods based on the Jeans analysis of the velocity moments profiles (Sanchis et al., 2004; Lokas et al., 2006), methods using models of the projected phase space distribution (Wojtak et al., 2009; Mamon et al., 2013) or dynamical models of the infall velocity profile (Falco et al., 2013) (for a comparison between a broad range of available methods see Old et al. (2014)). The discrepancy between the measured and the actual cluster mass may differ between the methods; therefore, our results cannot be regarded as a general prediction for all of them. However, the substantial mass discrepancy shown for the caustic technique provides strong motivation for detailed studies of this effect in all other kinematic methods.

2.7 Outlook

One of the main objectives of this thesis has been to describe systematic scatter in the caustic effect due to spherical assumptions in the case of aspherical clusters and filaments. As discussed in the introductory sections many methods besides caustics employ an isotropic framework for deriving masses of galaxy clusters. Analyses of the type presented here on any mass estimation technique might demonstrate how much of the current total scatter in masses can be attributed to triaxiality, and to what degree the implementation of a triaxial framework is worth the effort. Naturally the true cluster orientation remains a free parameter, but future techniques might help to constrain it and in that case masses could be determined to higher precision than what is currently possible.

Acknowledgments

I would like to sincerely thank Radoslaw Wojtak and Steen Hansen for helpful and patient supervision whenever needed, as well as a constructive and cooperative work on the paper that resulted from this thesis. I would also like to thank Daniel Gifford and Doron Lemze for helpfully answering questions regarding the caustic technique and for helpful comments.

Bibliography

- Ahn C. P., Alexandroff R., Allende Prieto C., Anders F., Anderson S. F., Anderton T., Andrews B. H., Aubourg É., Bailey S., Bastien F. A., et al. 2014, *ApJS*, 211, 17
- Allen S. W., Evrard A. E., Mantz A. B., 2011, *ARA&A*, 49, 409
- Allen S. W., Schmidt R. W., Fabian A. C., 2002, *MNRAS*, 334, L11
- Allgood B., Flores R. A., Primack J. R., Kravtsov A. V., Wechsler R. H., Faltenbacher A., Bullock J. S., 2006, *MNRAS*, 367, 1781
- Bartelmann M., 2010, *Classical and Quantum Gravity*, 27, 233001
- Binney J., Tremaine S., 2008, *Galactic Dynamics: Second Edition*. Princeton University Press
- Biviano A., Girardi M., 2003, *ApJ*, 585, 205
- Biviano A., Murante G., Borgani S., Diaferio A., Dolag K., Girardi M., 2006, *A&A*, 456, 23
- Biviano A., Rosati P., Balestra I., Mercurio A., Girardi M., Nonino M., Grillo C., Scodreggio M., Lemze D., Kelson D., Umetsu K., Postman M., Zitrin A., Czoske O., Ettori S., Fritz A., 2013, *A&A*, 558, A1
- Böhringer H., Werner N., 2010, *A&A Rev.*, 18, 127
- Carlstrom J. E., Holder G. P., Reese E. D., 2002, *ARA&A*, 40, 643
- Clowe D., De Lucia G., King L., 2004, *MNRAS*, 350, 1038
- Colberg J. M., Krughoff K. S., Connolly A. J., 2005, *MNRAS*, 359, 272
- Cuesta A. J., Prada F., Klypin A., Moles M., 2008, *MNRAS*, 389, 385
- Diaferio A., 1999, *MNRAS*, 309, 610
- Falco M., Hansen S. H., Wojtak R., Brinckmann T., Lindholmer M., Pandolfi S., 2013, *ArXiv e-prints*
- Franx M., Illingworth G., de Zeeuw T., 1991, *ApJ*, 383, 112
- Geller M. J., Diaferio A., Rines K. J., Serra A. L., 2013, *ApJ*, 764, 58
- Gifford D., Miller C., Kern N., 2013, *ApJ*, 773, 116
- Gifford D., Miller C. J., 2013, *ApJ*, 768, L32
- Hahn O., Carollo C. M., Porciani C., Dekel A., 2007, *MNRAS*, 381, 41
- Klypin A. A., Trujillo-Gomez S., Primack J., 2011, *ApJ*, 740, 102
- Komatsu E., Dunkley J., Nolte M. R., Bennett C. L., Gold B., Hinshaw G., Jarosik N., Larson D., Limon M., Page L., Spergel D. N., Halpern M., Hill R. S., Kogut A., Meyer S. S., Tucker G. S., Weiland J. L., Wollack E., Wright E. L., 2009, *ApJS*, 180, 330

- Lau E. T., Nagai D., Kravtsov A. V., Vikhlinin A., Zentner A. R., 2012, *ApJ*, 755, 116
- Lemze D., Broadhurst T., Rephaeli Y., Barkana R., Umetsu K., 2009, *ApJ*, 701, 1336
- Lemze D., Postman M., Genel S., Ford H. C., Balestra I., Donahue M., Kelson D., Nonino M., Mercurio A., Biviano A., Rosati P., Umetsu K., 2013, *ApJ*, 776, 91
- Libeskind N. I., Hoffman Y., Forero-Romero J., Gottlöber S., Knebe A., Steinmetz M., Klypin A., 2013, *MNRAS*, 428, 2489
- Limousin M., Morandi A., Sereno M., Meneghetti M., Ettori S., Bartelmann M., Verdugo T., 2013, *Space Sci. Rev.*, 177, 155
- Lokas E. L., Wojtak R., Gottlöber S., Mamon G. A., Prada F., 2006, *MNRAS*, 367, 1463
- Mamon G. A., Biviano A., Boué G., 2013, *MNRAS*, 429, 3079
- Mantz A., Allen S. W., Rapetti D., Ebeling H., 2010, *MNRAS*, 406, 1759
- Mantz A. B., Allen S. W., Morris R. G., Rapetti D. A., Applegate D. E., Kelly P. L., von der Linden A., Schmidt R. W., 2014, *ArXiv e-prints*
- Old L., Skibba R. A., Pearce F. R., Croton D., Muldrew S. I., Muñoz-Cuartas J. C., Gifford D., Gray M. E., von der Linden A., Mamon G. A., Merrifield M. R., Müller V., Pearson R. J., Tempel E., Tundo E., Wang Y. O., Wojtak R., 2014, *ArXiv e-prints*
- Pisani A., 1993, *MNRAS*, 265, 706
- Rapetti D., Allen S. W., Mantz A., Ebeling H., 2010, *MNRAS*, 406, 1796
- Riebe K., Partl A. M., Enke H., Forero-Romero J., Gottloeber S., Klypin A., Lemson G., Prada F., Primack J. R., Steinmetz M., Turchaninov V., 2011, *ArXiv e-prints*
- Rines K., Diaferio A., 2006, *AJ*, 132, 1275
- Rines K., Geller M. J., Diaferio A., Kurtz M. J., 2013, *ApJ*, 767, 15
- Rozo E., Wechsler R. H., Rykoff E. S., Annis J. T., Becker M. R., Evrard A. E., Frieman J. A., Hansen S. M., Hao J., Johnston D. E., Koester B. P., McKay T. A., Sheldon E. S., Weinberg D. H., 2010, *ApJ*, 708, 645
- Sanchis T., Lokas E. L., Mamon G. A., 2004, *MNRAS*, 347, 1198
- Saro A., Mohr J. J., Bazin G., Dolag K., 2013, *ApJ*, 772, 47
- Serra A. L., Diaferio A., Murante G., Borgani S., 2011, *Monthly Notices of the Royal Astronomical Society*, 412, 800
- Silverman B., 1986, *Monographs on statistics and applied probability*, 26
- Springel V., White S. D. M., Jenkins A., Frenk C. S., Yoshida N., Gao L., Navarro J., Thacker R., Croton D., Helly J., Peacock J. A., Cole S., Thomas P., Couchman H., Evrard A., Colberg J., Pearce F., 2005, *Nature*, 435, 629
- Vikhlinin A., Kravtsov A. V., Burenin R. A., Ebeling H., Forman W. R., Hornstrup A., Jones C., Murray S. S., Nagai D., Quintana H., Voevodkin A., 2009, *ApJ*, 692, 1060
- Vogelsberger M., Genel S., Springel V., Torrey P., Sijacki D., Xu D., Snyder G. F., Nelson D., Hernquist L., 2014, *ArXiv e-prints*
- Wojtak R., 2013, *A&A*, 559, A89
- Wojtak R., Lokas E. L., Mamon G. A., Gottlöber S., 2009, *MNRAS*, 399, 812
- Zemp M., Gnedin O. Y., Gnedin N. Y., Kravtsov A. V., 2011, *ApJS*, 197, 30

Chapter 3

Appendix

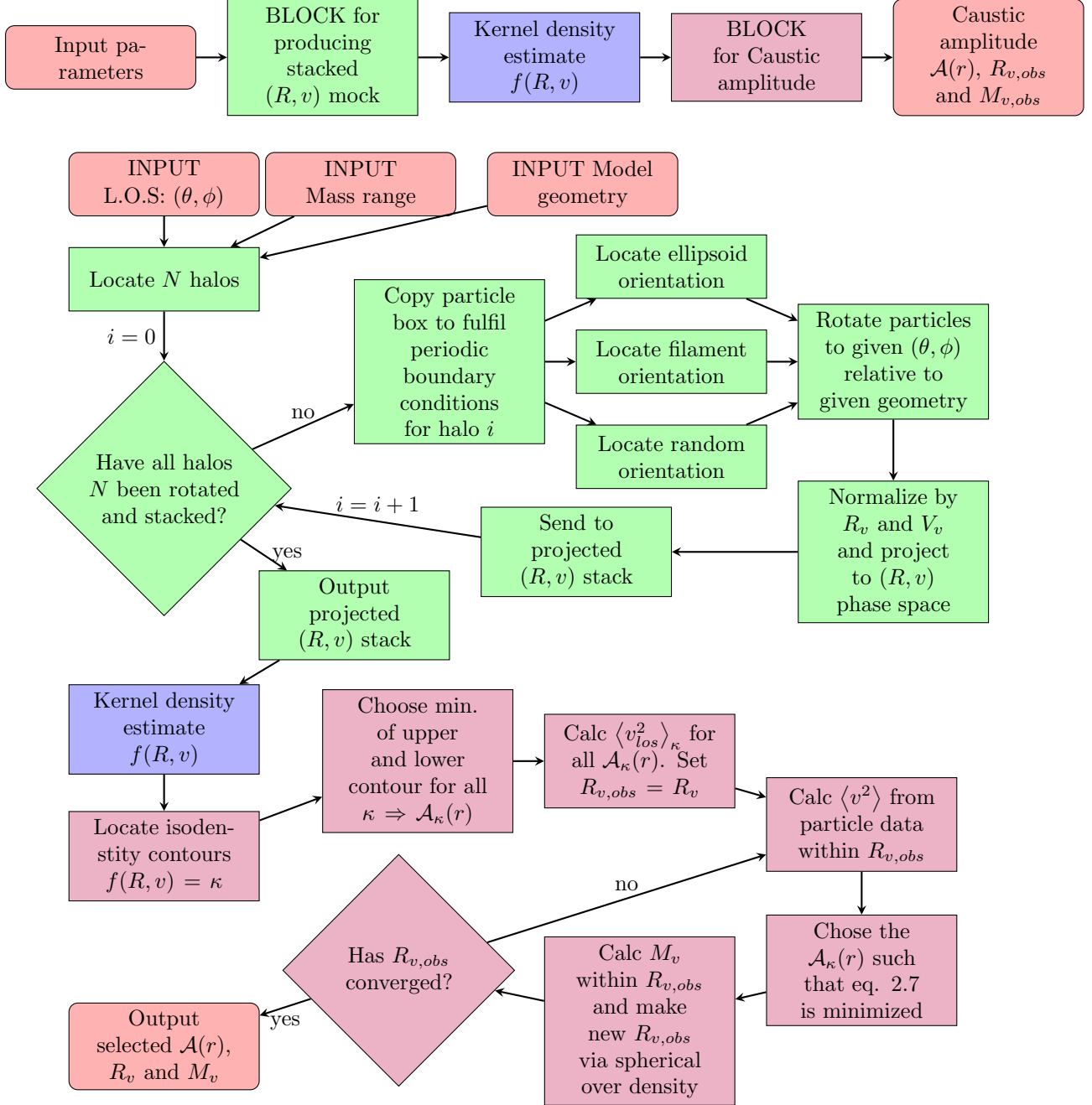


Figure 1: Flowchart describing the computational process in obtaining stacked mock phase-space diagrams and caustic amplitudes given number of input parameters. Overview is given in the top, and a more elaborate flowchart is given in the bottom with the same color coding. Note that all code to perform the above was made in Interactive Data Language (IDL).

Table 1: Values of triaxiality and mass estimates for the oblate and prolate substacks of the *ellipsoidal stacks*. The three 'Triaxiality' columns show the intermediate to major axis ratio b/a , the minor to major axis ratio c/a and the triaxiality parameter T for each of the stacks in questions for particles within R_v . The 'Mean mass' columns show the mean of 10,000 mass measurements obtained from 10,000 interpolations of each panel in Fig. 2.4 and Fig. 2.5 for 10,000 directions randomly distributed on the sphere. The 'Scatter in masses' columns show the scatter defined as the standard deviation of the 10,000 mass measurements. The 'Max/min mass' columns show the ratio of the maximum mass estimate to the minimum mass estimate for each panel in Fig. 2.4 and Fig. 2.5. All mass values are normalized by M_s .

Stack name	Triaxiality			Mean mass			Scatter in masses			Max/min mass		
	b/a	c/a	T	$1 R_v$	$2 R_v$	$3 R_v$	$1 R_v$	$2 R_v$	$3 R_v$	$1 R_v$	$2 R_v$	$3 R_v$
$[1, 2] \times 10^{14} M_\odot h^{-1}$												
Prolate Stack	0.66	0.60	0.89	1.02	1.03	1.00	0.14	0.14	0.18	1.67	1.78	1.83
Oblate Stack	0.92	0.72	0.31	0.98	1.01	1.10	0.14	0.20	0.23	1.74	1.82	1.88
$\geq 2 \times 10^{14} M_\odot h^{-1}$												
Prolate Stack	0.66	0.61	0.89	1.03	1.11	1.19	0.19	0.26	0.43	2.04	2.41	3.08
Oblate Stack	0.90	0.68	0.34	1.02	1.06	1.13	0.20	0.26	0.46	2.12	2.18	2.61

Table 2: Caustic mass estimates of the low mass bin *ellipsoidal stack* within $1 R_v$, $2 R_v$ and $3 R_v$ for varying line of sight, normalized by the estimate from the spherical stack. Columns represent θ angles, rows represent ϕ angles, both are indicated in bold in the table and both are in degrees. These values are also represented as the top 3 panels of Fig. 2.4.

$1 R_v$	0	15	30	45	60	75	90
90	0.75	0.76	0.80	0.86	0.91	0.95	0.95
75	0.75	0.76	0.81	0.87	0.93	0.97	0.99
60	0.75	0.77	0.83	0.91	0.99	1.04	1.06
45	0.75	0.78	0.86	0.95	1.05	1.13	1.13
30	0.75	0.78	0.89	1.01	1.12	1.21	1.25
15	0.75	0.79	0.91	1.04	1.16	1.25	1.29
0	0.75	0.80	0.91	1.05	1.18	1.26	1.30
$2 R_v$	0	15	30	45	60	75	90
90	0.74	0.76	0.80	0.87	0.93	0.96	0.98
75	0.74	0.76	0.80	0.88	0.94	0.99	1.01
60	0.74	0.77	0.82	0.91	1.01	1.07	1.07
45	0.75	0.77	0.84	0.95	1.08	1.19	1.22
30	0.75	0.78	0.87	1.01	1.16	1.35	1.38
15	0.74	0.78	0.90	1.05	1.25	1.37	1.42
0	0.74	0.79	0.90	1.06	1.23	1.39	1.46
$3 R_v$	0	15	30	45	60	75	90
90	0.65	0.67	0.70	0.78	0.88	0.93	0.99
75	0.66	0.67	0.70	0.79	0.87	0.98	1.00
60	0.66	0.69	0.73	0.85	0.97	1.04	1.06
45	0.66	0.69	0.77	0.90	1.12	1.29	1.32
30	0.66	0.68	0.80	1.02	1.21	1.49	1.54
15	0.65	0.69	0.82	1.06	1.36	1.57	1.61
0	0.65	0.69	0.82	1.07	1.27	1.58	1.60

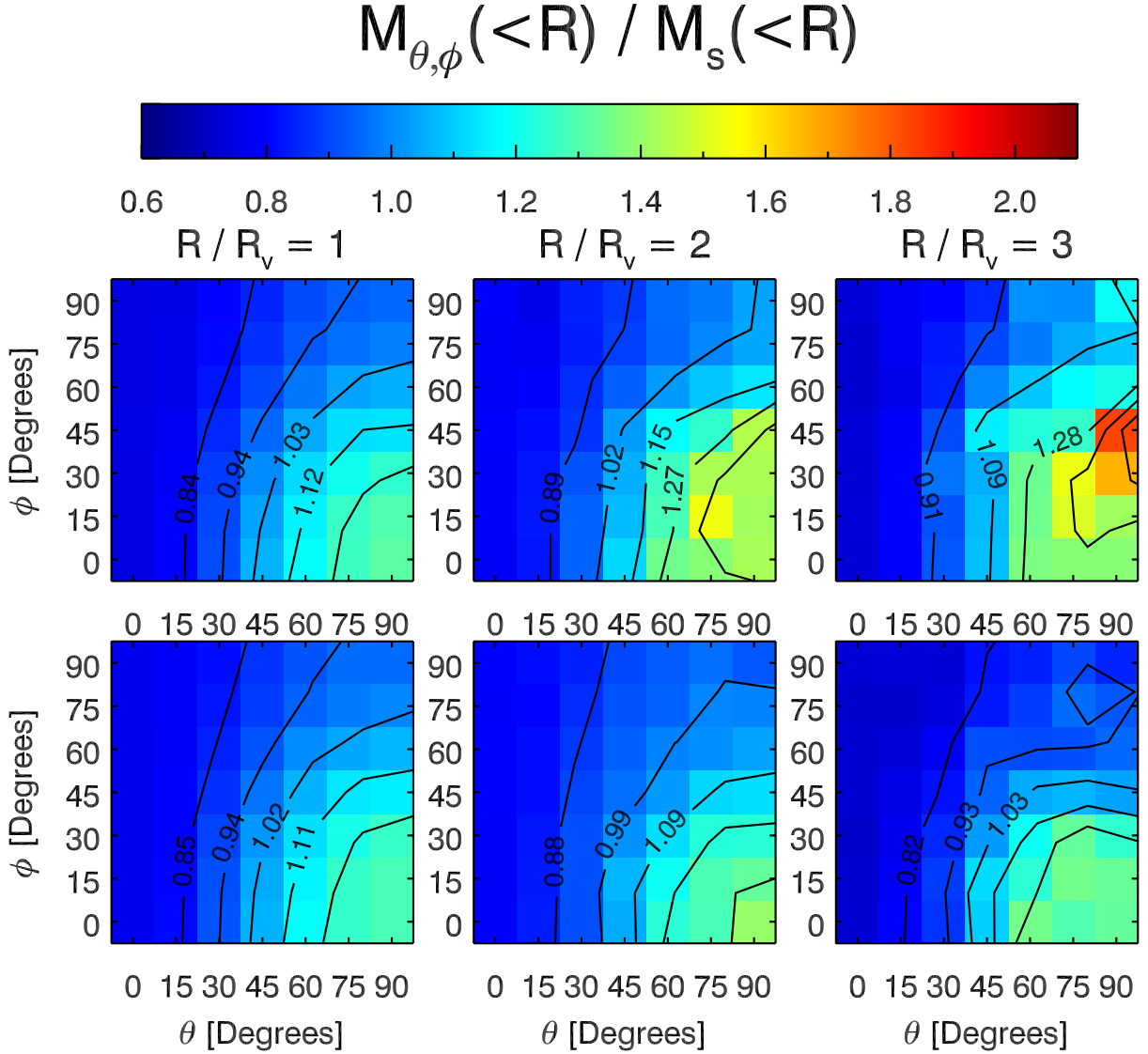


Figure 2: Effect of the cluster orientation on the caustic mass estimate for the 40 most oblate (top panels) and prolate (bottom panels) clusters as sorted by triaxiality T for the low mass bin. The panels show the mass estimates as a function of the orientation, relative to the mass inferred from the *spherical stack*. The three columns show results for three choices of radii. θ and ϕ indicate the line of sight in question, defined for each stack in Fig. 2.1. For the top panels ($90^\circ, 0^\circ$) represents the sight line along the major axis, ($90^\circ, 90^\circ$) represents light line along minor axis and entire left side at $\theta = 0^\circ$ represents the minor axis for any ϕ . The color for any (θ, ϕ) indicates the value of the mass estimate as indicated on the linear colorbar. The lines in each panel show equally-spaced isodensity contours.

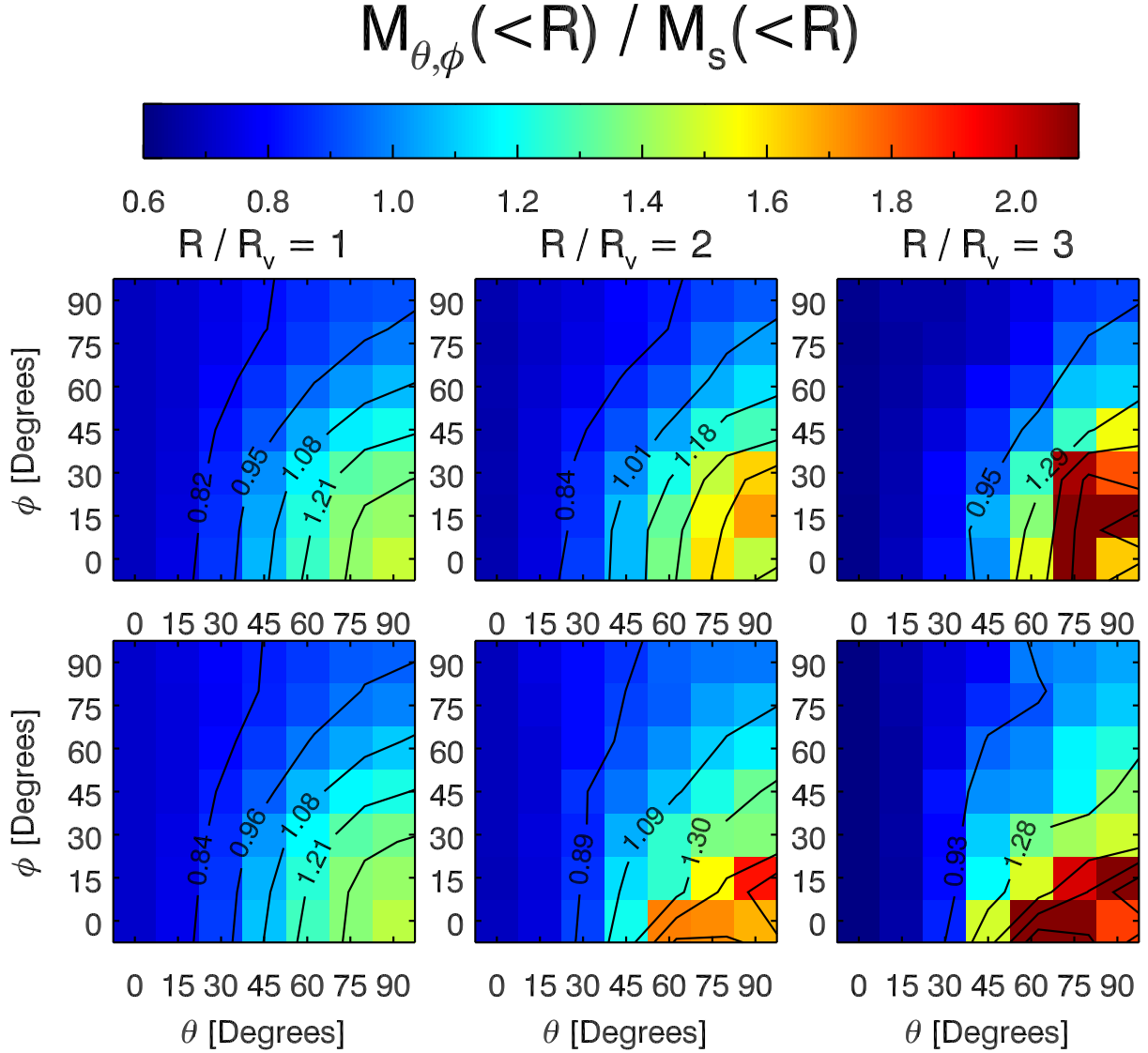


Figure 3: Effect of the cluster orientation on the caustic mass estimate for the 19 most oblate (top panels) and prolate (bottom panels) clusters as sorted by triaxiality T for the high mass bin. The panels show the mass estimates as a function of the orientation, relative to the mass inferred from the *spherical stack*. The three columns show results for three choices of radii. θ and ϕ indicate the line of sight in question, defined for each stack in Fig. 2.1. For the top panels ($90^\circ, 0^\circ$) represents the sight line along the major axis, ($90^\circ, 90^\circ$) represents light line along minor axis and entire left side at $\theta = 0^\circ$ represents the minor axis for any ϕ . The color for any (θ, ϕ) indicates the value of the mass estimate as indicated on the linear colorbar. The lines in each panel show equally-spaced isodensity contours.

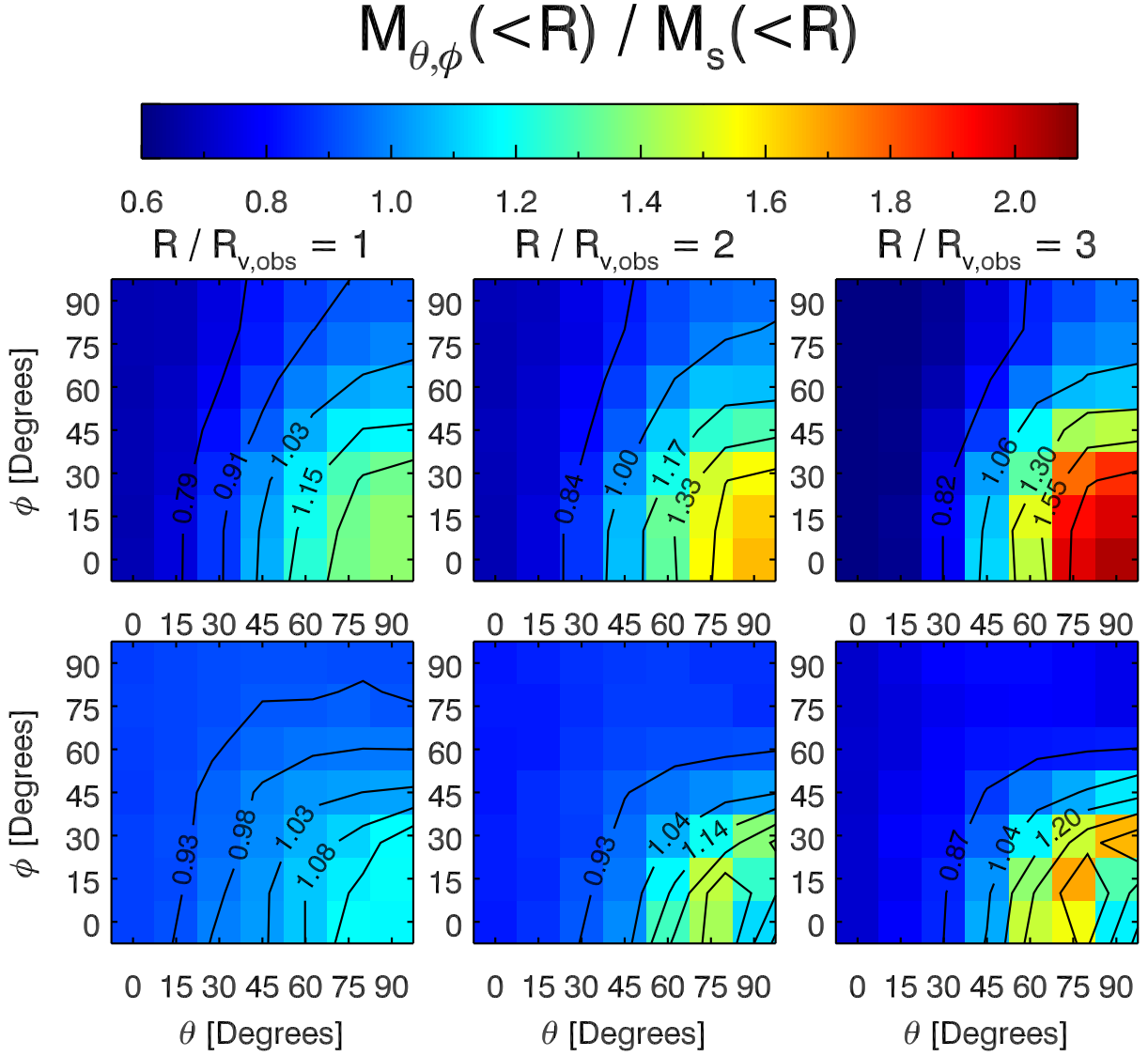


Figure 4: Effect of the cluster orientation on the caustic mass estimates for the low mass bin *ellipsoidal* and *filamentary stacks* evaluated at the observed virial radii $R_{v,obs}$. The panels show the mass estimates as a function of the orientation, relative to the mass inferred from the *spherical stack*. The three columns show results for three choices of radii. θ and ϕ indicate the line of sight in question, defined for each stack in Fig. 2.1. For the top panels ($90^\circ, 0^\circ$) represents the sight line along the major axis, ($90^\circ, 90^\circ$) represents light line along minor axis and entire left side at $\theta = 0^\circ$ represents the minor axis for any ϕ . The color for any (θ, ϕ) indicates the value of the mass estimate as indicated on the linear colorbar. The lines in each panel show equally-spaced isodensity contours.

Table 3: Caustic mass estimates of the low mass bin *filamentary stack* within $1 R_v$, $2 R_v$ and $3 R_v$ for varying line of sight, normalized by the estimate from the spherical stack. Columns represent θ angles, rows represent ϕ angles, both are indicated in bold in the table and both are in degrees. These values are also represented as the bottom 3 panels of Fig. 2.4.

$1 R_v$	0	15	30	45	60	75	90
90	0.91	0.91	0.93	0.93	0.94	0.93	0.93
75	0.91	0.91	0.93	0.95	0.94	0.95	0.94
60	0.91	0.91	0.94	0.96	0.98	0.98	0.98
45	0.91	0.92	0.96	0.99	1.02	1.03	1.04
30	0.91	0.93	0.96	1.01	1.05	1.09	1.14
15	0.91	0.92	0.98	1.02	1.08	1.12	1.14
0	0.91	0.93	0.99	1.02	1.08	1.13	1.14
$2 R_v$	0	15	30	45	60	75	90
90	0.85	0.86	0.89	0.90	0.90	0.88	0.88
75	0.85	0.85	0.88	0.90	0.90	0.90	0.87
60	0.85	0.85	0.89	0.91	0.91	0.91	0.92
45	0.85	0.88	0.90	0.93	0.96	0.99	1.02
30	0.85	0.88	0.90	0.95	1.04	1.16	1.28
15	0.85	0.87	0.92	0.97	1.13	1.39	1.19
0	0.85	0.88	0.93	0.99	1.22	1.35	1.09
$3 R_v$	0	15	30	45	60	75	90
90	0.74	0.78	0.83	0.84	0.84	0.82	0.78
75	0.74	0.76	0.79	0.81	0.81	0.80	0.79
60	0.75	0.77	0.81	0.84	0.84	0.84	0.85
45	0.74	0.80	0.81	0.88	0.95	1.02	1.11
30	0.75	0.82	0.83	0.93	1.11	1.36	1.46
15	0.75	0.79	0.85	0.99	1.30	1.54	1.19
0	0.75	0.81	0.85	1.03	1.39	1.39	1.06

Table 4: Caustic mass estimates of the high mass bin *ellipsoidal stack* within $1 R_v$, $2 R_v$ and $3 R_v$ for varying line of sight, normalized by the estimate from the spherical stack. Columns represent θ angles, rows represent ϕ angles, both are indicated in bold in the table and both are in degrees. These values are also represented as the top 3 panels of Fig. 2.5.

$1 R_v$	0	15	30	45	60	75	90
90	0.70	0.73	0.77	0.82	0.87	0.92	0.93
75	0.71	0.73	0.77	0.83	0.89	0.95	0.99
60	0.70	0.73	0.79	0.87	0.96	1.03	1.08
45	0.71	0.73	0.82	0.93	1.06	1.16	1.20
30	0.70	0.74	0.85	1.01	1.17	1.30	1.35
15	0.70	0.75	0.87	1.05	1.23	1.37	1.40
0	0.70	0.75	0.87	1.08	1.27	1.38	1.45
$3 R_v$	0	15	30	45	60	75	90
90	0.69	0.73	0.77	0.82	0.88	0.95	0.99
75	0.70	0.72	0.77	0.83	0.89	0.98	1.01
60	0.69	0.73	0.78	0.87	0.96	1.04	1.12
45	0.70	0.73	0.82	0.92	1.05	1.18	1.26
30	0.69	0.74	0.84	1.00	1.19	1.39	1.43
15	0.70	0.74	0.85	1.07	1.27	1.51	1.58
0	0.69	0.74	0.86	1.07	1.36	1.50	1.54
$3 R_v$	0	15	30	45	60	75	90
90	0.62	0.65	0.69	0.74	0.84	0.91	1.00
75	0.63	0.65	0.70	0.76	0.84	0.96	0.99
60	0.62	0.66	0.72	0.82	0.91	1.03	1.08
45	0.63	0.66	0.74	0.87	1.02	1.22	1.27
30	0.62	0.66	0.77	0.96	1.24	1.60	1.67
15	0.63	0.66	0.79	1.04	1.35	1.78	1.85
0	0.63	0.67	0.81	1.07	1.53	1.90	1.85

Table 5: Caustic mass estimates of the high mass bin *filamentary stack* within $1 R_v$, $2 R_v$ and $3 R_v$ for varying line of sight, normalized by the estimate from the spherical stack. Columns represent θ angles, rows represent ϕ angles, both are indicated in bold in the table and both are in degrees. These values are also represented as the bottom 3 panels of Fig. 2.5.

$1 R_v$	0	15	30	45	60	75	90
90	0.87	0.88	0.91	0.92	0.95	0.94	0.95
75	0.87	0.88	0.92	0.95	0.95	0.96	0.97
60	0.87	0.90	0.94	0.97	1.00	1.00	1.01
45	0.87	0.90	0.95	1.00	1.04	1.06	1.09
30	0.87	0.91	0.96	1.03	1.08	1.12	1.13
15	0.87	0.91	0.96	1.04	1.12	1.14	1.10
0	0.87	0.91	0.96	1.04	1.13	1.11	1.05
$3 R_v$	0	15	30	45	60	75	90
90	0.87	0.86	0.89	0.90	0.94	0.94	0.95
75	0.86	0.87	0.91	0.93	0.94	0.96	0.97
60	0.86	0.89	0.92	0.95	0.97	0.97	0.99
45	0.86	0.88	0.93	0.96	1.00	1.03	1.09
30	0.87	0.89	0.94	0.99	1.05	1.13	1.16
15	0.87	0.90	0.93	0.99	1.15	1.26	1.14
0	0.87	0.90	0.94	0.99	1.14	1.21	0.98
$3 R_v$	0	15	30	45	60	75	90
90	0.84	0.82	0.85	0.85	0.88	0.88	0.90
75	0.81	0.83	0.85	0.89	0.89	0.91	0.90
60	0.82	0.86	0.86	0.92	0.93	0.91	0.94
45	0.82	0.82	0.87	0.91	0.99	1.08	1.12
30	0.84	0.82	0.87	0.96	1.15	1.29	1.27
15	0.83	0.84	0.88	0.98	1.34	1.26	1.09
0	0.83	0.84	0.90	1.01	1.23	1.22	0.87

FACULTY OF SCIENCE
UNIVERSITY OF COPENHAGEN



Co-author statement

In accordance with the thesis rules applicable at SCIENCE, a co-author statement must be available from each of the authors concerning the thesis student's share of the work in articles, manuscripts etc. Written in collaboration with co-authors are included in the thesis report or as appendices to the thesis report.

The thesis student is responsible for procuring the co-author statements on time. The thesis will not be evaluated until the co-author statements are available. The co-author statement must be submitted to the supervisor along with the thesis.

1. General information

Name: Jacob Svensmark Civ. reg. no.: 2206861013

Principal supervisor: Steen H. Hansen

Department: The Niels Bohr Institute

2. This co-author statement applies to the following article og manuscript

Effect of asphericity in caustic mass estimates of galaxy clusters, arxiv:1405.0284

3. Statement concerning individual elements

The scope of the thesis student's contribution to the articles is assessed on the basis of the following scale:

- A. Has contributed to the collaboration (0-33%).
- B. Has made a significant contribution (34-66%).
- C. Has essentially performed this work independently (67-100%).

1. Formulation at the idea stage of the basic scientific issue based on theoretical questions which are sought clarified, including a summary of the issue in relation to questions for which it is deemed that answers can be provided by conducting analyses or conducting specific experiments or surveys, respectively.	<input type="checkbox"/> A <input checked="" type="checkbox"/> B <input type="checkbox"/> C
2. Planning of the experiments/analyses and design of the survey methodology in such a way that the questions posed as a whole can reasonably be expected to be answered, including choide of methodology and independent development of methodology.	<input type="checkbox"/> A <input type="checkbox"/> B <input checked="" type="checkbox"/> C
3. Involvement in the analysis work or the specific experimentation/survey, respectively.	<input type="checkbox"/> A <input type="checkbox"/> B <input checked="" type="checkbox"/> C
4. Presentation and interpretation of the results achieved in the form of article(s).	<input type="checkbox"/> A <input type="checkbox"/> B <input checked="" type="checkbox"/> C

1/2

4. Co-author's signature

27.05.2014

Date

Radosław Wojtak

Name

postdoctoral researcher

Title

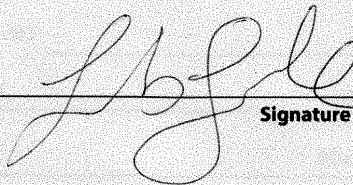
Radosław Wojtak

Signature

5. Thesis student's signature

27.05.2014

Date



Signature

FACULTY OF SCIENCE
UNIVERSITY OF COPENHAGEN



Co-author statement

In accordance with the thesis rules applicable at SCIENCE, a co-author statement must be available from each of the authors concerning the thesis student's share of the work in articles, manuscripts etc. Written in collaboration with co-authors are included in the thesis report or as appendices to the thesis report.

The thesis student is responsible for procuring the co-author statements on time. The thesis will not be evaluated until the co-author statements are available. The co-author statement must be submitted to the supervisor along with the thesis.

1. General information

Name: Jacob Svensmark Civ. reg. no.: 2206861013

Principal supervisor: Steen H. Hansen

Department: The Niels Bohr Institute 

2. This co-author statement applies to the following article og manuscript

Effect of asphericity in caustic mass estimates of galaxy clusters, arxiv:1405.0284

3. Statement concerning individual elements

The scope of the thesis student's contribution to the articles is assessed on the basis of the following scale:

- A. Has contributed to the collaboration (0-33%).
- B. Has made a significant contribution (34-66%).
- C. Has essentially performed this work independently (67-100%).

1.	Formulation at the idea stage of the basic scientific issue based on theoretical questions which are sought clarified, including a summary of the issue in relation to questions for which it is deemed that answers can be provided by conducting analyses or conducting specific experiments or surveys, respectively.	<input type="checkbox"/> A <input type="checkbox"/> B <input checked="" type="checkbox"/> C
2.	Planning of the experiments/analyses and design of the survey methodology in such a way that the questions posed as a whole can reasonably be expected to be answered, including choide of methodology and independent development of methodology.	<input type="checkbox"/> A <input type="checkbox"/> B <input checked="" type="checkbox"/> C
3.	Involvement in the analysis work or the specific experimentation/survey, respectively.	<input type="checkbox"/> A <input type="checkbox"/> B <input checked="" type="checkbox"/> C
4.	Presentation and interpretation of the results achieved in the form of article(s).	<input type="checkbox"/> A <input type="checkbox"/> B <input checked="" type="checkbox"/> C

1/2

4. Co-author's signature

26 05 14
Date

STEEN HANSEN
Name

Dr.
Title


Signature

5. Thesis student's signature

26.05.2014
Date


Signature

